Experimental Generation and Computational Modeling of Intracellular pH Gradients in Cardiac Myocytes

Pawel Swietach,* Chae-Hun Leem,[†] Kenneth W. Spitzer,[‡] and Richard D. Vaughan-Jones*

*Burdon Sanderson Cardiac Science Centre, University Laboratory of Physiology, Oxford OX1 3PT, United Kingdom; [†]Department of Physiology, University of Ulsan College of Medicine, Seoul 138-040, Korea; and [‡]Nora Eccles Harrison Cardiovascular Research and Training Institute, University of Utah, Salt Lake City, Utah 84112 USA

ABSTRACT   It is often assumed that pH_i is spatially uniform within cells. A double-barreled microperfusion system was used to apply solutions of weak acid (acetic acid, CO_2) or base (ammonia) to localized regions of an isolated ventricular myocyte (guinea pig). A stable, longitudinal pH_i gradient (up to 1 pH_i unit) was observed (using confocal imaging of SNARF-1 fluorescence). Changing the fractional exposure of the cell to weak acid/base altered the gradient, as did changing the concentration and type of weak acid/base applied. A diffusion-reaction computational model accurately simulated this behavior of pH_i. The model assumes that H_i^+ movement occurs via diffusive shuttling on mobile buffers, with little free H^+ diffusion. The average diffusion constant for mobile buffer was estimated as 33×10^{-7} cm²/s, consistent with an apparent H_i^+ diffusion coefficient, D_H^{app}, of 14.4×10^{-7} cm²/s (at pH_i 7.07), a value two orders of magnitude lower than for H^+ ions in water but similar to that estimated recently from local acid injection via a cell-attached glass micropipette. We conclude that, because H_i^+ mobility is so low, an extracellular concentration gradient of permeant weak acid readily induces pH_i nonuniformity. Similar concentration gradients for weak acid (e.g., CO_2) occur across border zones during regional myocardial ischemia, raising the possibility of steep pH_i gradients within the heart under some pathophysiological conditions.

INTRODUCTION

Intracellular pH (pH_i) is a major modulator of the electrical and contractile properties of cardiac cells (e.g., Bountra and Vaughan-Jones, 1989; Harrison et al., 1992; Komukai et al., 2002; Choi et al., 2000). Displacements of cardiac pH_i from its resting value of ~7.1 will occur physiologically, for example, during extracellular acid-base disturbances (Ellis and Thomas, 1976), or in response to changes in the metabolic workload placed on the heart (Bountra et al., 1988; Elliott et al., 1994). The most common displacement is an intracellular acidosis. Depending on conditions, this can have either a positive or a negative inotropic effect (Bountra and Vaughan-Jones, 1989). A major cause of the negative inotropy is a reduction in the Ca^{2+} sensitivity of troponin-C whereas one cause of the positive inotropy is a rise of cytoplasmic Ca^{2+}, secondary to the stimulation of sarcolemmal Na^+-H^+ exchange. Under pathophysiological conditions such as myocardial ischemia, a severe intracellular acidosis (of up to 1 pH unit) is also known to occur (e.g., Garlick et al., 1979; Allen and Orchard, 1987), and this contributes significantly to a rapid loss of contractile function. Efficient regulation of intracellular pH is thus essential to the maintenance of normal cardiac function.

Changes of pH within the cytoplasmic compartment of a myocyte are usually assumed to be uniform. This notion has been challenged recently, however, with the realization that intracellular H^+ mobility is remarkably low, about two orders of magnitude lower than in water (Vaughan-Jones et al., 2002; Zaniboni et al., 2003). This is because the cytoplasmic compartment is highly buffered and most of the buffers, by virtue of their size, are poorly mobile. Almost all spatial H^+ movement within a cell is likely to occur via a diffusive shuttling on intracellular buffers, with little free diffusion of the H^+ ion itself. Low H_i^+ mobility raises the prospect of spatial nonuniformity of pH_i occurring, at least transiently, in cardiac and other cells in response to local acid/base disturbances. Such nonuniformity has been documented in experiments where pH_i was imaged confocally in epithelial (Stewart et al., 1999) and neuronal cells (Schwiening and Willoughby, 2002; Willoughby and Schwiening, 2002), after activation of transmembrane H^+-equivalent movement through membrane transporters and channels. By far the largest pH_i nonuniformity (up to 1 pH_i unit) has been reported in isolated ventricular myocytes, and myocyte pairs, exposed to extracellular concentration gradients of membrane-permeant weak acid or base (Spitzer et al., 2000; Swietach and Vaughan-Jones, 2004). Such weak-acid gradients may be comparable in size to those occurring for CO_2 during regional myocardial ischemia (Case et al., 1979; Cascio et al., 1992). The physiological consequences of pH_i heterogeneity within a cell are not known but, in the case of the cardiac myocyte, they are likely to include contractile and electrical dysfunction.

In this work, we have employed a dual microperfusion apparatus to localize a known concentration of extracellular weak acid or base (such as CO_2, acetic acid, and ammonia) at the surface of an enzymically isolated ventricular myocyte, while confocally imaging pH_i using intracellular carboxy-SNARF-1 fluorescence. As mentioned above,

(Spitzer et al., 2000), this approach generates longitudinal pH_i gradients. We explore the characteristics of these gradients by varying the degree of exposure of the cell to the weak acid/base, and by varying its concentration. We develop a diffusion-reaction model of H_i^+ mobility, based on the mobility of intracellular buffer molecules of given concentration and acid-dissociation constant (pK). The model is an extension of previous algorithms for intracellular H^+ diffusion (Vaughan-Jones et al., 2002; Swietach et al., 2003; Zaniboni et al., 2003). We use the model, in combination with our experimental results, to assess the buffer hypothesis of H_i^+ mobility. We also use our data to estimate the apparent intracellular H^+ ion diffusion coefficient, D_H^{app}, and we compare this value with that estimated recently from the direct injection of acid through a cell-attached glass micropipette (Vaughan-Jones et al., 2002; Zaniboni et al., 2003).

The implications for cellular pH_i regulation of a low H_i^+ mobility, and the factors that control the size and shape of pH_i gradients formed during the localization of extracellular weak acid or base are discussed.

METHODS

Myocyte isolation

Ventricular myocytes were isolated from guinea pigs ($\approx$400 g, killed by cervical dislocation in accordance with UK Home Office guidelines) using a combination of mechanical and enzymatic dispersion (0.7 mg/mL collagenase, Roche, Mannheim, Germany, and 0.04 mg/mL protease, Sigma, Poole, UK). Cells were stored in culture medium at room temperature. See also Leem et al. (1999) for details. All myocytes used in this study were rod shaped, with well-defined striations and did not contract spontaneously.

Superfusion system

All experiments were carried out in a 400-μl Plexiglas chamber mounted on an inverted confocal microscope (Leica DM IRBE). The chamber was constantly supplied with superfusate (Hepes- or CO_2/bicarbonate-buffered normal Tyrode), maintained at 37°C by a feedback resistance heater. A suction tube, connected to a water pump, maintained a low level of solution in the chamber, and hence a fast rate of solution exchange. Before cells were allowed to settle in the superfusion chamber, the coverslip (number-1, Chance Proper, Birmingham, UK) was coated with 200 μl poly-L-lysine (Sigma) to enhance cell adhesion.

Dual microperfusion system

To create regional differences of pH_i in single myocytes, we used a microperfusion system (Spitzer and Bridge 1989, Spitzer et al., 2000). It consists of a short ($\approx$7 mm) length of custom-made double-barreled square glass tubing (Wilmad Glass, Buena, NJ) attached to a micromanipulator. The internal width of each barrel is $\sim$250 μm, with a 70-μm glass septum separating the barrels. Two microstreams, driven by hydrostatic pressure from elevated solution reservoirs, simultaneously flowed from both barrels, creating a sharp interstream boundary. For optimum compartmentalization of solutions, both microstream flows were set to $\sim$30 μl/s. The tip of the double-barreled pipette was positioned <300 μm from a myocyte such that the microstreams were roughly perpendicular to the cell's longitudinal axis ($\pm$10°). This minimizes turbulent solution flow over the cell, which could otherwise lead to an irregular and diffuse microstream boundary (Spitzer et al., 2000).

To test the quality of the microstream boundary, normal Tyrode was run through both microstreams, one of which contained 100 μM fluorescein (Molecular Probes, Eugene, OR). Fluorescence was excited by the 488-nm line of an Argon laser and acquired confocally at >510 nm emission (see Fig. 1). The boundary was quantified as the width over which fluorescence falls from 95% to 5%. For a typical flow rate, the average boundary width was 8.7 $\pm$ 1.6 μm ($n = 9$).

Once the double-barreled micropipette was lowered into the bath and placed near a myocyte, the cell was superfused with the dual microstream. The solution boundary could be moved by means of the fine control of a micromanipulator that held the double-barreled pipette. The boundary could be inspected during the experiment from the transmission image produced by the confocal microscope. To aid visualization of the boundary, 20 mM sucrose was added to one of the microstream solutions. This creates a small difference in refractive index between the two solutions that emphasizes the boundary region when viewed with transmitted light. The sucrose had no effect on intracellular fluorescence, pH_i or pH_o, and it exerts a minimal osmotic effect on the cell. For details of the dual microstream assembly, see Spitzer et al. (2000).

Confocal measurement of pH_i

Cells were suspended in normal Hepes-buffered (10 mM) DMEM culture medium in the experimental chamber (at room temperature, with no flow)
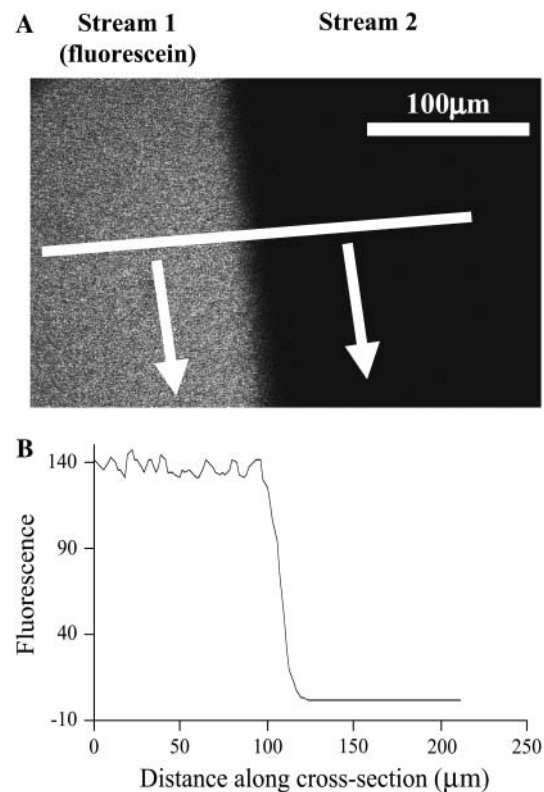

FIGURE 1 Dual microperfusion. (A) Confocal imaging (excitation wavelength 488 nm) of two microstreams emerging from the double-barreled micropipette. The left-hand side microstream contained 100 μM fluorescein (emission wavelength 510 nm). No fluorophore was included in the right microstream. Arrows indicate direction of solution flow. Horizontal white line shows distance over which the fluorescence profile in panel B was measured. (B) The longitudinal fluorescence profile (arbitrary units) plotted perpendicular to the microstream boundary suggests a boundary width <10 μm (measured as the distance between 5 and 95% signal).

into which was added the esterified form of the pH-sensitive fluorophore, carboxy-SNARF-1-AM, at a final concentration of 10 μM (from a 1.7-mM stock solution in DMSO). Cells were exposed to the dye for 10 min. Note that the presence of intracellular carboxy-SNARF-1 does not significantly affect H_i^+ mobility (Vaughan-Jones et al., 2002; Zaniboni et al., 2003), as opposed to, for example, the Ca^{2+} dye, Fura-2, which greatly enhances Ca^{2+} mobile buffering capacity hence Ca_i^{2+} mobility (Gabso et al., 1997). The dye-loading solution was then flushed away and normal superfusion commenced at 37°C. Intracellular carboxy-SNARF-1 was excited by an Argon laser at 514 nm and fluorescence was imaged confocally at 580 and 640 nm using a Leica ×40, 1.25 numerical aperture, oil immersion, plano-apochromat objective lens. For details of confocal measurement of pH_i with carboxy-SNARF-1, see Vaughan-Jones et al. (2002) and Zaniboni et al. (2003). Calibration of ratiometric carboxy-SNARF-1 fluorescence was performed using the nigericin method (Thomas et al., 1979) once every four months, as described previously (Vaughan-Jones et al., 2002).

Data acquisition for pH_i was performed in ''*xyt*'' mode (two spatial dimensions in the horizontal plane, recorded over time) with two-frame averaging to reduce noise. The resulting bitmaps (at 256 × 256 pixel resolution) were stored every 2.1 s. Using in-house macros, the entire stack was separated into the fluorescence signal at 580 nm, 640 nm, and the transmission image. The ratio of the 580- and 640-nm fluorescence images was then used to calculate the spatial distribution of pH_i using calibration curves. These macros could also plot pH_i time courses in selected regions of interest (ROIs) or pH_i profiles along any plotting vector.

Solutions and drugs

The superfusate and one of the microstreams contained Hepes- or CO_2/bicarbonate-buffered normal Tyrode solution. The other microstream also contained a weak base (ammonium chloride) or weak acid (sodium acetate or high CO_2 and bicarbonate).

Hepes-buffered solution

pH of all solutions was adjusted to 7.4 with NaOH or HCl. i), Normal Tyrode (in mM): NaCl (135), KCl (4.5), $MgCl_2$ (1), $CaCl_2$ (2), Hepes (20), glucose (11); ii), NH_4Cl-containing Tyrode: NH_4Cl (5, 10, or 20) added with a corresponding reduction of NaCl (i.e., 130, 125, and 115, respectively), KCl (4.5), $MgCl_2$ (1), $CaCl_2$ (2), Hepes (20), glucose (11), sucrose (20); iii), 80 mM acetate Tyrode (in mM): NaCl (55), NaAcetate (80), KCl (4.5), $MgCl_2$ (1), $CaCl_2$ (2), Hepes (20), glucose (11), sucrose (20).

CO₂/bicarbonate-buffered solution

pH of all solutions was 7.4. i), Normal Tyrode (in mM): NaCl (119), $NaHCO_3$ (22), KCl (4.5), $MgCl_2$ (1), $CaCl_2$ (2), glucose (11), bubbled with 5% CO_2 at 37°C; ii), 20 mM ammonium Tyrode (in mM): NaCl (99), NH_4Cl (20), $NaHCO_3$ (22), KCl (4.5), $MgCl_2$ (1), $CaCl_2$ (2), glucose (11), bubbled with 5% CO_2 at 37°C; iii), high CO_2 Tyrode (in mM): NaCl (56), $NaHCO_3$ (88), KCl (4.5), $MgCl_2$ (1), $CaCl_2$ (2), glucose (11), bubbled with 20% CO_2 at 37°C. To avoid CO_2 leakage from bicarbonate-buffered solution, CO_2-impermeable tubing (Norton, UK) was used to connect the glass solution reservoirs to the superfusion chamber.

Drugs

Acetazolamide was obtained from Sigma. Cariporide (HOE-642, Scholz et al., 1995) was kindly supplied by Dr. H. W. Kleemann of Aventis (Germany).

Modeling intracellular pH gradients

Computer simulations were designed to explain pH_i phenomena obtained experimentally in terms of the behavior of intracellular buffers. The mechanism generating a pH_i gradient during local exposure to weak acid/

base is analyzed in the Discussion, and schematic diagrams of the underlying solute movements are presented in Fig. 12. The fundamental features of the model are a low intracellular apparent proton diffusion coefficient (D_H^{app}) and a buffering capacity that is divided into mobile (β_{mob}) and fixed (β_{fix}) components (Vaughan-Jones et al., 2002; Zaniboni et al., 2003). D_H^{app} may be expressed as the product of mobile buffer diffusion coefficient (D_{mob}) and the ratio of mobile/total buffering capacity (Junge and McLaughlin, 1987; Irving et al., 1990; Swietach et al., 2003):

$$D_H^{app} = D_{mob} \times \frac{\beta_{mob}}{\beta_{mob} + \beta_{fix}}. \qquad (1)$$

Models used in this work adopted an intrinsic buffering system in accordance with Leem et al. (1999) who proposed two buffer populations of pK 7.57 and 6.03 and concentration 29.38 and 84.22 mM, respectively. The former buffer was assumed to be mobile, whereas the latter was considered predominantly fixed (Zaniboni et al., 2003). Because mobile and fixed buffering capacity varies with pH_i, the value of D_H^{app} (Eq. 1) is also predicted to be pH_i dependent (Zaniboni et al., 2003). Indeed, a rise of D_H^{app} with pH has been reported from experiments on extruded molluscan cytoplasm (Al-Baldawi and Abercrombie, 1992). Comparison of values derived for D_H^{app} in this work was therefore made at a common pH_i. Where necessary, a value for D_H^{app} could be adjusted to a given pH_i by recalculating the relevant values for β_{mob} and β_{fix} (Eq. 1). The diffusion-reaction algorithm used in the computational simulations assumed a constant value for D_{mob} (33 × 10^{-7} cm²/s). Using this value, the D_H^{app} predicted for a resting pH_i of 7.07 (Eq. 1) would be ~15 × 10^{-7} cm²/s. The value selected for D_{mob} is similar to that estimated recently for the guinea-pig ventricular myocyte (26 × 10^{-7} cm²/s; Zaniboni et al., 2003).

The diffusion-reaction problem can be represented mathematically as the sum of intracellular diffusion, $\nabla(D\nabla u)$, intracellular reaction, $R(u)$, and transmembrane flux, $T(u,v)$, components,

$$\frac{\partial u}{\partial t} = \nabla(D \cdot \nabla u) + R(u) + T(u, v). \qquad (2)$$

Array ''u'' is a vector in which each element represents the intracellular concentration of participating solutes:

$$\begin{pmatrix} H^+ & HM & M & HF & F & CO_2 & HCO_3^- & NH_4^+ & NH_3 & HAc & Ac^- \\ 1 & 2 & 3 & 4 & 5 & 6 & 7 & 8 & 9 & 10 & 11 \end{pmatrix}$$

Similarly, array ''v'' describes the extracellular concentration of these solutes. In the vector above, symbols M and F represent the lumped mobile and fixed buffer, respectively. Each species is assigned a diffusion coefficient according to Table 1. The reaction component of Eq. 2 is defined as follows (see Table 1 for values of rate constants, k_{on}, and acid dissociation constants, K).

$$R_1 = R_3 + R_5 + R_7 + R_9 + R_{11}$$
$$R_2 = -(k_{on,buff} \cdot K_{mob} \cdot u_{HM} - k_{on,buff} \cdot u_H \cdot u_M)$$
$$R_3 = (k_{on,buff} \cdot K_{mob} \cdot u_{HM} - k_{on,buff} \cdot u_H \cdot u_M)$$
$$R_4 = -(k_{on,buff} \cdot K_{fix} \cdot u_{HF} - k_{on,buff} \cdot u_H \cdot u_F)$$
$$R_5 = (k_{on,buff} \cdot K_{fix} \cdot u_{HF} - k_{on,buff} \cdot u_H \cdot u_F)$$
$$R_6 = -(k_{hydr} \cdot u_{CO2} - k_{hydr}/K_{carb} \cdot u_H \cdot u_{HCO3})$$
$$R_7 = (k_{hydr} \cdot u_{CO2} - k_{hydr}/K_{carb} \cdot u_H \cdot u_{HCO3})$$
$$R_8 = -(k_{on,amm} \cdot K_{amm} \cdot u_{NH4} - k_{on,amm} \cdot u_H \cdot u_{NH3})$$
$$R_9 = (k_{on,amm} \cdot K_{amm} \cdot u_{NH4} - k_{on,amm} \cdot u_H \cdot u_{NH3})$$
$$R_{10} = -(k_{on,ac} \cdot K_{ac} \cdot u_{HAc} - k_{on,ac} \cdot u_H \cdot u_{Ac})$$
$$R_{11} = (k_{on,ac} \cdot K_{ac} \cdot u_{HAc} - k_{on,ac} \cdot u_H \cdot u_{Ac}).$$

TABLE 1 Table of constants and parameters

Symbol	Definition	Value* unless stated otherwise	Reference
R	Universal gas constant	8.31 J mol^{-1} K^{-1}	
F	Faraday constant	96,500 C mol^{-1}	
T_B	Body temperature	37°C, 310 K	–
Z	Ionic charge	Integer	
ε	$\exp(-z \cdot V_m \cdot F/R \cdot T)$	–	
pH$_o$	Normal extracellular pH	7.4	
pH$_r$	Resting intracellular pH	7.07	
V_m	Membrane potential	−80 mV	This study
L	Cell length (guinea pig)	125 μm (mean)	
W	Cell width (guinea pig)	20 μm (mean)	
H	Cell height (guinea pig)	10 μm (mean)	
η	Surface area correction due to infolding	1.69	Satoh et al., 1996
C_{mob}	Concentration of pooled ''mobile buffer''	29.38 mM	
C_{fix}	Concentration of pooled ''fixed buffer''	84.22 mM	Leem et al., 1999 (guinea pig)
K_{mob}	''Mobile buffer'' dissociation constant	$10^{-7.57}$	
K_{fix}	''Fixed buffer'' dissociation constant	$10^{-6.03}$	
K_{amm}	Ammonium dissociation constant	$10^{-9.03}$	Klocke et al., 1972
K_{ac}	Acetate dissociation constant	$10^{-4.528}$	Harned and Hickney, 1937
K_{carb}	Equilibrium constant of CO_2 hydration	$10^{-6.12}$	
S_{CO2}	CO_2 solubility in water	0.0247 M atm^{-1}	Leem and Vaughan-Jones, 1998
k_{hydr}	Spontaneous CO_2 hydration rate	0.14 s^{-1}	
k_{hydr}^{cat}	Catalyzed CO_2 hydration rate	0.36 s^{-1}	
$k_{on,buff}$	Fast buffer protonation rate constant	$\sim10^{10}$ M^{-1} s^{-1}	
$k_{on,amm}$	Ammonia protonation rate constant	4.3×10^{10} M^{-1} $^{-1}$	Eigen, 1964
$k_{on,ac}$	Acetate protonation rate constant	4.5×10^{10} M^{-1} $^{-1}$	
D_H	Free proton diffusion coefficient	12×10^{-5} cm^2/s	Swietach et al., 2003
D_{mob}	Mobile buffer diffusion coefficient	33×10^{-7} cm^2/s	This study
D_{fix}	Fixed buffer diffusion coefficient	0.0	
D_{CO2}	CO_2 diffusion coefficient	1.105×10^{-5} cm^2/s	Reid et al., 1987
D_{HCO3}	Bicarbonate diffusion coefficient	7.7×10^{-6} cm^2/s	
D_{amm}	Ammonia and ammonium diffusion coefficient	1.27×10^{-5} cm^2/s	Swietach et al., 2003
D_{ac}	Acetate and acetic acid diffusion coefficient	7.08×10^{-6} cm^2/s	
P_{CO2}	CO_2 membrane permeability constant	0.56 cm/s	Forster, 1969
P_{NH3}	Ammonia membrane permeability constant	54.5×10^{-4} cm/s	K. W. Spitzer, R. D. Vaughan-Jones, and
P_{HAc}	Acetic acid membrane permeability constant	38×10^{-4} cm/s	C. H. Leem, unpublished data
P_{NH4}	Ammonium membrane permeability constant	1.408×10^{-7} cm/s	Leem et al., 1999
P_{Ac}	Acetate membrane permeability constant	6.77×10^{-9} cm/s	

Although intrinsic buffering is often referred to as instantaneous, these buffers have a finite rate constant of protonation ($k_{on,buff}$). The value of the protonation rate constant varies with chemical entity, but it is typically as fast as 10^{10} M^{-1}s^{-1} (see typical organic compounds in Eigen, 1964) for intrinsic buffers. It appears that taking any value $>10^9$ M^{-1}s^{-1} produces a converging solution, therefore it is not critical to use an accurate value for k_{on} for rapid buffers. The carbonic buffer is a so-called ''slow buffer''. The rate-limiting step is the hydration of CO_2 to carbonic acid, which then dissociates to HCO_3^- and H^+. In the presence of physiological quantities of carbonic anhydrase, the intracellular rate constant of hydration in the ventricular myocyte is 0.36 s^{-1}. In the absence of enzyme or under its inhibition with acetazolamide, the hydration slows to 0.14 s^{-1} (Leem and Vaughan-Jones, 1998).

Component $T(u,v)$ of Eq. 2 describes flux between the intracellular and extracellular compartments. The membrane permeability to intracellular intrinsic buffers is set to zero for isolated myocytes. The flux of protons was programmed according to the activity of membrane transporters. If the flux was small, it could be ignored because the dual microperfusion simulations often lasted only 1 min. The major proton transporter expressed in guinea-pig myocytes is Na$^+$-H$^+$ exchange (NHE) (Leem et al., 1999; Yamamoto et al., 2004). The flux data for this transporter (J^{NHE}) as a function of pH$_i$ were fitted with a sigmoid curve based on the data of Yamamoto et al. (2004):

$$J^{NHE}(\text{mEq/l/min}) = -47.110 \cdot \frac{[H^+]^{2.134}}{[H^+]^{2.134} + (10^{-6.376})^{2.134}}.$$

The proton-equivalent flux on CHE (Cl$^-$-OH$^-$ exchange) is much smaller (Leem et al., 1999) and could be ignored. However, to produce a steady-state pH$_i$ of 7.07, it is necessary to account for an inward H$^+$ flux of +1.5 mEq/l/min to oppose J^{NHE}. In simulations involving considerable net alkalosis, NHE activity is greatly depressed. Under these conditions, proton efflux was assumed to be negligible. Similarly, in the presence of a pharmacological block of NHE using the drug cariporide, proton efflux was set to zero. The guinea-pig sarcolemma also expresses Na$^+$-HCO$_3^-$ cotransport (NBC) and Cl$^-$-HCO$_3^-$ anion exchange. Most simulations presented in this work, however, involved CO_2/HCO$_3^-$-free superfusates. Under these conditions, bicarbonate transport is inactive. Only during partial exposure of cells to CO_2 is it likely that NBC mediates some pH$_i$ recovery from acidosis. This flux was not, however, included in the model because, during intracellular acidosis, it is much smaller than NHE-mediated flux (Leem et al., 1999).

Membrane flux of weak acids and bases (CO_2, NH$_3$, NH$_4^+$, Ac$^-$, HAc) was formulated by using passive electrochemical (for charged species) or chemical (for uncharged species) flux equations described in Leem et al. (1999). To incorporate compartmentalization of extracellular weak acid/base

due to the dual microperfusion apparatus, extracellular concentrations of the solutes (array ''v'') were multiplied by a step function taking values of 1 where the boundary was exposed to the solute and zero otherwise.

The type of equation represented by Eq. 2 is a nonlinear system of partial differential equations (PDEs). In problems where the longitudinal concentration profiles of solutes are more important than radial gradients, cell geometry can be simplified to a slab and solved with one spatial dimension. Indeed, myocyte length typically exceeds myocyte width and height by a factor of >6. For solving Eq. 2, it is assumed that the second spatial derivatives in the y- and z-directions are nil. This mandates the use of PDE solvers, such as pdepe, (Mathworks, Natick, MA) that handle one space variable only, but allow for nonlinearity in the reaction and permeation terms, as required for pH_i simulations. Simulations were run for 60 s of dual microperfusion. The PDE solver is conditioned for a slab divided into a large number (>50) of finite elements. For convenience, these elements are set to equal length. It is necessary to estimate the surface area of these elements to derive total transmembrane flux. Satoh et al. (1996) calculated that the surface area/volume ratio for an entire guinea-pig myocyte is ~0.5 μm^{-1}.

This value was used to estimate the surface area and volume for each element. Note that the terminal elements at the ends of the cell have an additional surface over which transmembrane flux can occur.

Statistics

Summarized results are expressed as means ± SE.

RESULTS

Generating longitudinal pH_i gradients with ammonium

Effect of boundary position

The guinea-pig myocyte shown in the transmission image at the top of Fig. 2 A was partially perfused with ammonium at
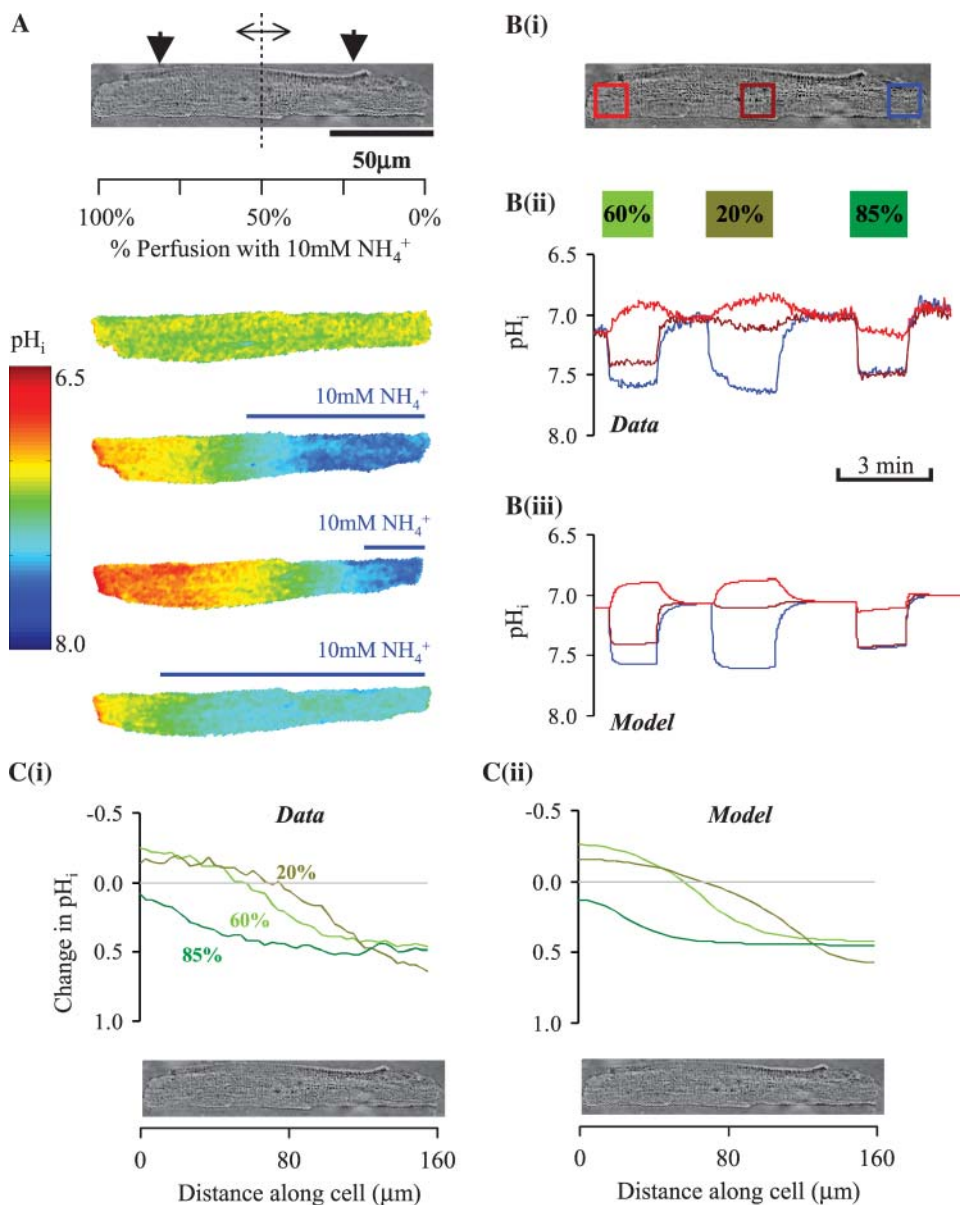

FIGURE 2   Partial exposure to ammonia. (A, *top panel*) Transmission image of a guinea-pig myocyte; vertical arrows show direction of microstream flow; vertical dashed line shows position of solution boundary; horizontal double-headed arrow shows direction in which solution boundary was moved during the course of the experiment. (A, *bottom panel*) Time-averaged confocal images collected in the steady-state period before and during 60, 20, and 85% partial exposure of the myocyte to 10 mM ammonium under Hepes-buffered conditions. (Bi) Transmission image of the myocyte showing the location of ROIs within which pH_i time courses were averaged. (Bii) Experimental data showing pH_i time courses in the three ROIs during the entire partial perfusion experiment. (Biii) Simulation of experimental data obtained from diffusion-reaction algorithms, assuming no sarcolemmal NHE activity and no carbonic buffer. (Ci) Experimental data for the longitudinal end-to-end pH_i profiles plotted along the length of the cell during 60, 20, and 85% partial perfusion with 10 mM ammonium. (Cii) These longitudinal pH_i profiles have been simulated using diffusion-reaction algorithms.

three different boundary positions. The microstreams were directed roughly at right angles to the myocyte to minimize turbulence, thus maximizing the localization of extracellular weak acid or base (Spitzer et al., 2000; see also Methods). The left microstream contained normal Tyrode, and the right contained Tyrode plus 10 mM ammonium chloride. All solutions were Hepes buffered. During dual microperfusion, the spatial distribution of pH_i was measured and averaged over a 30-s period in the steady state. Specimen confocal images are shown in Fig. 2 *A*. The uppermost confocal image shows that pH_i was uniform when the cell was uniformly superfused with normal Tyrode. The other images show that, during partial exposure to ammonium, a large and stable longitudinal pH_i gradient was generated, with the exposed (right-hand) region of the myocyte becoming alkaline relative to the nonexposed (left-hand) region. Furthermore, the size of the pH_i gradient was affected by the size of the region exposed to ammonium chloride. No radial gradients of pH_i were detected.

Three ROIs were defined, one at each end, and one in the center of the myocyte (illustrated in Fig. 2 *Bi*). Dual microperfusion was performed three times, with boundary positions (and hence exposure to ammonium) at 60%, 20%, and 85% along the length of the cell. The pH_i time courses recorded within the ROIs (Fig. 2 *Bii*) indicate that a longitudinal pH_i gradient was established within ~30 s. As described previously (Spitzer et al., 2000), the gradient is generated by transmembrane influx of NH_3 in the exposed region, leading rapidly to a local rise of pH_i as intracellular NH_3 combines with protons forming NH_4^+ ions. Because intracellular H^+ mobility is low, spatial diffusion of protons from less alkaline regions is insufficient to dissipate the alkaline microdomain, leading to a smooth longitudinal pH_i gradient. During the course of the experiment shown in Fig. 2 *Bii*, there was a small acidifying drift of baseline pH in the three ROIs. During short episodes of dual microperfusion (up to 2 min) such drift was minimal (<0.1 units).

Fig. 2 *Ci* shows longitudinal pH_i profiles, generated by averaging signals (over a 20-s period of steady-state pH_i) during the dual microperfusion. The smoothness of the pH_i profiles suggests it is generated by a diffusive process. To test this hypothesis, the H^+ diffusion-reaction algorithm was run to simulate the experiment (assuming no NHE activity and assuming Hepes buffer in the microstreams). Note that the model assumes a low value for intracellular D_H^{app} (15.0×10^{-7} cm²/s at resting pH_i), in line with that reported previously in the cardiac myocyte (12.1×10^{-7} cm²/s at pH_i 6.95; see Methods). The time courses of pH_i change predicted in the three ROIs are shown in Fig. 2 *Biii*. These match closely the amplitude and kinetics of the experimental data. Moreover, the sigmoidal longitudinal profile of pH_i in the steady state is adequately reproduced (Fig. 2 *Cii*). The modeling also confirms that changing boundary position affects both the size and shape of the longitudinal pH_i gradient.

The results of Fig. 2 suggest that longitudinal pH_i gradients can be easily manipulated by the simple maneuver of altering boundary position. Additional experiments were performed with a higher dose of ammonium (20 mM) to produce larger pH_i gradients. All solutions were again Hepes buffered and guinea-pig myocytes were selected to have similar dimensions. In total, 80 myocytes were dually perfused at boundary positions ranging from no exposure to ammonium, to almost complete exposure. Once pH_i had reached a steady state, it was averaged (over 20 s) within two ROIs (10×10 μm) centered axially at 10% away from the cell ends. Results were then binned for every 10% change in boundary position and plotted in Fig. 3 *A*. The proximal ROI
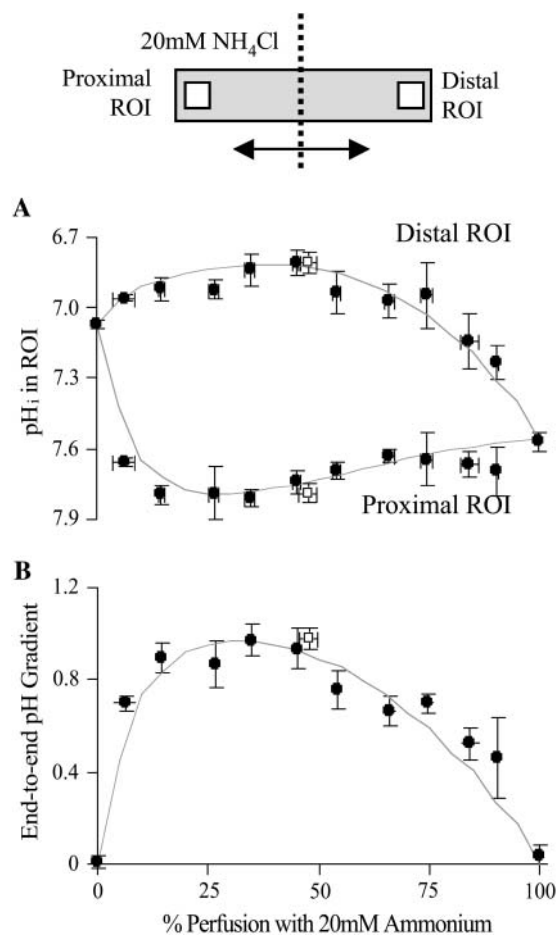
FIGURE 3 Degree of fractional exposure to ammonia determines pH_i-gradient size. (*A*) The pH_i in the proximal and distal ROIs (placed axially at 10% away from the cell ends; see schematic diagram at top) plotted as a function of percentage exposure of a cell to 20 mM ammonium under Hepes-buffered conditions. Solid symbols represent binned data ($n = 4, 2, 13, 6, 9, 9, 11, 9, 7, 4, 2, 10$) from experiments performed in the absence of cariporide (NHE active). Open symbols ($n = 8$) represent experiments performed in the presence of 30 μM cariporide. The continuous lines are model predictions from the diffusion-reaction algorithms (no carbonic buffer and no sarcolemmal NHE activity). (*B*) End-to-end pH_i gradients calculated as the difference between the proximal and distal ROI pH_i. Model predictions are shown by the continuous curves.

was always on the same side as the ammonium-containing microstream. The difference in pH_i between the two ROIs was defined as the end-to-end pH_i gradient, as plotted in Fig. 3 B. In some experiments (*open symbols*; $n = 8$), 30 μM cariporide was included in the two microstreams, to inhibit sarcolemmal NHE, but it exerted no significant effect on either the time course of pH_i change in an ROI, or on the end-to-end pH_i gradient.

The continuous curves shown in Fig. 3 are model results, derived for a standard cell partially perfused with ammonium from 0 to 100% exposure. Both experiment and model indicate that the relationship between pH_i-gradient amplitude and fractional exposure to ammonium is biphasic, with no gradient occurring at zero or 100% exposure, and a maximal gradient at ~30% exposure. A full analysis of the mechanism of pH_i-gradient generation during dual microperfusion is presented in the Discussion.

Effect of cell geometry

The typical length of guinea-pig myocytes studied in this work was between 120 and 130 μm. It was difficult to perform experiments on longer myocytes due to their poor adhesion to the superfusion chamber. Very short myocytes (<60 μm) were not always suitable either, because the width of the microstream boundary (~8 μm) then became significant compared to the length of the cell. To explore more fully the relationship between cell length and the size of the longitudinal pH_i gradient, the computational model was used. This seemed to be a reasonable approach, as the model had reproduced well the kinetics and amplitude of pH_i changes during shifts in boundary position. Two parameters were varied simultaneously: cell length (0–250 μm) and boundary position (0–100%). The concentration of ammonium was set at 20 mM. Cell width and height were not investigated, as these dimensions vary less among myocytes. Because radial gradients are negligible compared with longitudinal gradients (e.g., Fig. 2 A), it is likely that width and height are not a major variable in pH_i-gradient formation.

Results of two-parameter modeling are shown as a contour map (Fig. 4). For the same dose of ammonium, longitudinal pH_i gradients were predicted to be as small as 0.1 pH units for short cells (e.g., 20-μm long) and to rise to over 1 pH unit for long cells (e.g., 150-μm long). Furthermore, peak pH_i gradients were predicted to occur for a much smaller degree of ammonium perfusion in long cells compared to short cells. Thus cell length is likely to be an important factor determining the shape and size of the pH_i gradient.

Effect of ammonium concentration

Increasing the extracellular concentration of ammonium in whole-cell superfusion increases the intracellular alkalosis (Roos and Boron, 1981; Leem et al., 1999). This may also be expected to occur in partially perfused cells, possibly
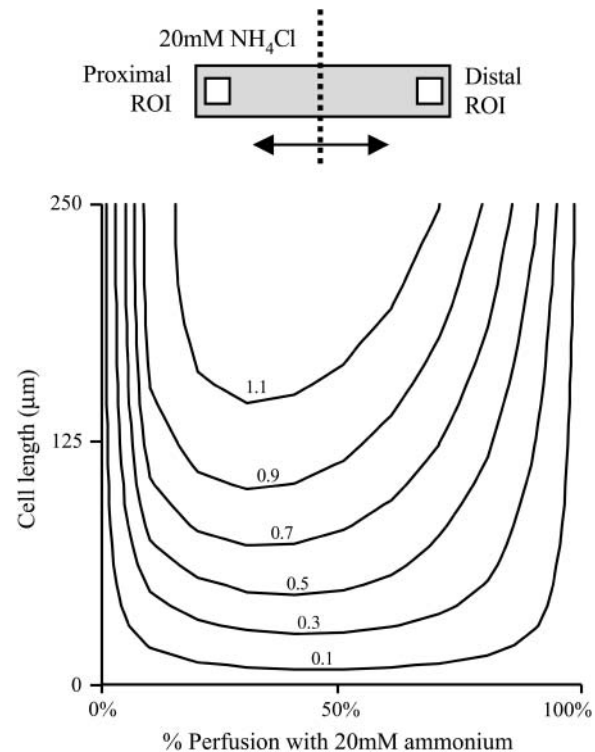

FIGURE 4 Effect of cell length on pH_i gradient. Contour map of modeling results, showing the relationship between cell-length (*vertical axis*), fractional exposure of cell to 20 mM NH$_4$Cl (*horizontal axis*), and the ensuing end-to-end pH_i gradient. Modeling protocol is summarized in the schematic diagram at the top. The simulations were performed assuming Hepes-buffered conditions (i.e., no carbonic buffer) and no sarcolemmal NHE activity.

resulting in larger end-to-end pH_i gradients. Indeed, this was observed experimentally in guinea-pig myocytes, partially superfused with ammonium chloride. Fig. 5 A shows data averaged for pH_i in proximal and distal ROIs (as defined previously in Fig. 3) during 50 ± 10% partial exposures to 5, 10, and 20 mM ammonium. Fig. 5 B shows the end-to-end pH_i gradients calculated from Fig. 5 A. Higher doses of extracellular ammonium produced larger longitudinal pH_i gradients. The continuous curves plotted in Fig. 5, A and B, denote the predictions obtained from the mathematical algorithm demonstrating that, once again, the results were well fit by the model.

Effect of varying apparent intracellular H$^+$ diffusion coefficient

In an intact cell, experimental manipulation of D_H^{app} is very difficult. To gain insight into how changing the apparent intracellular diffusion coefficient for H$^+$, NH$_3$, or NH$_4^+$ may influence the spatial distribution of pH_i, the effect of changing these diffusion parameters was simulated using the diffusion-reaction model. H$_i^+$ mobility was manipulated by changing the mobile buffer diffusion coefficient (D_{mob}).
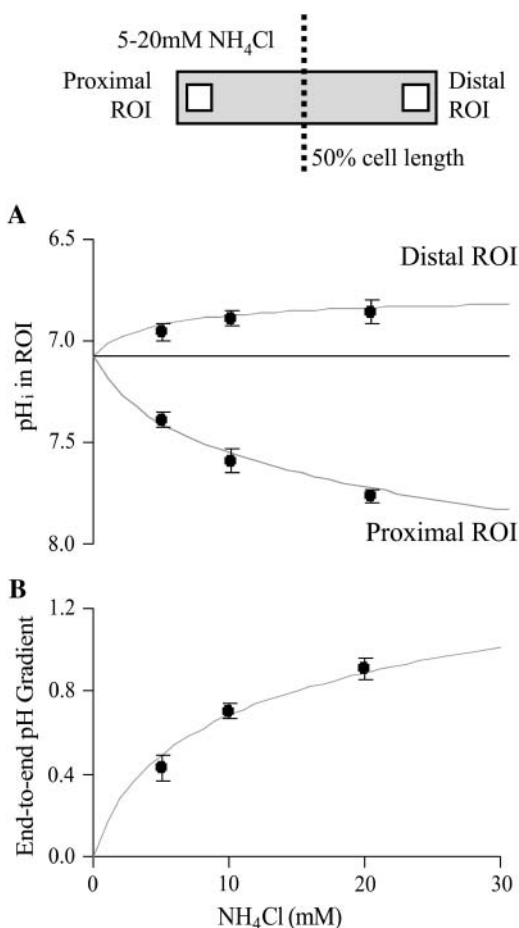
FIGURE 5 Effect of NH$_4$Cl concentration on pH$_i$ gradient. (*A*) Summary of experimental data showing pH$_i$ in the proximal and distal ROI (as shown in schematic diagram at *top*) during ~50% partial exposure to different concentrations of ammonium (n = 5, 6, 22), performed under Hepes-buffered conditions. Most experiments were performed in the absence of cariporide. In eight cells (exposed to 20 mM ammonium), the microstreams contained 30 μM cariporide to inhibit NHE. The effect of cariporide on pH$_i$ nonuniformity was, however, not significant, thus drug-free and drug-containing data were pooled. Continuous curves show model simulations performed for 50% exposure to different doses of ammonium (0–30 mM) in the absence of carbonic buffer and the absence of sarcolemmal NHE activity. (*B*) End-to-end pH$_i$ gradients calculated as the difference between the proximal and distal ROI pH$_i$. Model predictions are shown by the continuous curves.

Equation 1 indicates that D_H^{app} should be proportional to D_{mob}. Simulations assumed superfusion with Hepes-buffered solutions and no sarcolemmal NHE activity.

The range of D_{mob} tested in the model was between zero and 2.5 × 10^{-4} cm^2/s. This was equivalent to a D_H^{app} range from 0 to 1.1 × 10^{-4} cm^2/s at resting pH$_i$ (β_{mob}/β_{tot} = 0.45 at pH$_i$ 7.07; Eq. 1). Fig. 6 *Ai* shows the predicted pH$_i$ in proximal and distal ROIs for a model cell of length 125 μm and width 20 μm, during 50% exposure to 20 mM ammonium. In Fig. 6 *Aii*, the predicted end-to-end pH$_i$ gradient has been plotted versus D_H^{app}. The solid symbol represents the experimentally derived end-to-end pH$_i$

gradient for 50% partial perfusion with 20 mM ammonium (from Fig. 5 *B*). This has been plotted versus the value of D_H^{app} measured previously from pipette acid-loading experiments (Zaniboni et al., 2003). Because that estimate was 12.1 × 10^{-7} cm^2/s at a mean pH$_i$ of 6.95, the value adopted in Fig. 6 was assumed to be slightly higher, 15.0 × 10^{-7} cm^2/s for pH$_i$ 7.07, given that D_H^{app} is likely to increase with a rise in pH (Al-Baldawi and Abercrombie, 1992; Zaniboni et al., 2003). Due to the steepness of the predicted relationship between D_H^{app} and pH$_i$ gradient (Fig. 6 *Aii*), the experimentally measured longitudinal pH$_i$-gradient size (*solid symbol*; 0.908 ± 0.052 pH units, n = 22) translates to a predicted D_H^{app} range from 12.8 × 10^{-7} to 16.4 × 10^{-7} cm^2/s with a mean value of 14.4 × 10^{-7} cm^2/s. This narrow range of D_H^{app} suggests that the dual microperfusion method is an accurate means of assessing the low mobility of H$_i^+$. The validity of using the dual microperfusion approach is further strengthened by the finding that D_H^{app} estimated from pipette acid-loading experiments, corrected to pH 7.07, lies in the range predicted from Fig. 6 *Aii*.

The predicted decrease in the longitudinal pH$_i$ gradient for an increase in D_H^{app} illustrates the dissipative effect on local pH$_i$ microdomains of a raised proton mobility. In Fig. 6 *Aii*, the upper value for D_H^{app} used in the model (1.1 × 10^{-4} cm^2/s) is similar to the value for the proton diffusion coefficient in pure water (Vanysek, 1999). Because the pH$_i$ gradient predicted with such a value of D_H^{app} approaches zero, it is unlikely that unbuffered proton diffusion is a major mechanism for the bulk movement of acid within the cell.

Effect of varying intracellular NH$_3$/NH$_4^+$ diffusion coefficient

As mentioned above, the diffusion-reaction model utilizes a theoretical value for the intracellular diffusion coefficients of NH$_3$ and NH$_4^+$. For simplicity, these have been lumped into a single constant (D_{amm}, assumed to be 1.27 × 10^{-5} cm^2/s, Swietach et al., 2003). It is therefore important to establish the extent to which the value assumed for D_{amm} affects the pH$_i$ gradient predicted during dual microperfusion. The value for D_{amm} was drawn from biophysical tables (Vanysek, 1999), modified for temperature using the Arrhenius equation, and corrected for diffusion of unbuffered solute in the intracellular compartment (using a correction factor proposed by Kushmerick and Podolsky, 1969). Originally calculated from radio-labeled Na$^+$ and K$^+$ studies in skeletal muscle, the latter factor is ~0.5 and may result from macromolecular crowding within the cell, which effectively halves the volume available for diffusion. To assess the importance of the value assumed for D_{amm}, the diffusion-reaction model was used to examine the relationship between D_{amm} and the resulting longitudinal pH$_i$ gradient. The model was run for a 50% partial perfusion with 20 mM ammonium, assuming Hepes-buffered conditions and no NHE activity.

FIGURE 6 pH_i gradient depends on D_H^{app} and D_{amm}. (Ai) Continuous lines plot predictions of the diffusion-reaction algorithm for the relationship between pH_i in the ROIs (protocol illustrated in schematic diagram at top) and the apparent proton diffusion coefficient (D_H^{app}) generated by varying D_{mob} in the model (assuming 50% exposure to 20 mM NH_4Cl, no carbonic buffer and no sarcolemmal NHE). ROIs were placed axially at 10% from the cell ends. Note the logarithmic horizontal scale. Diamond symbols refer to pH_i measured in experiments ($n = 22$). These are the same experimental data as shown in Fig 5 for 20 mM NH_4Cl. The data are plotted versus the value measured for D_H^{app} (pH_i 7.07) by Zaniboni et al. (2003). (Aii) Size of end-to-end pH_i gradient calculated from panel Ai. (Bi) Results of modeling pH_i in proximal and distal ROIs obtained for a range of values for ammonia/ammonium diffusion coefficient (D_{amm}), assuming 50% exposure to 20 mM NH_4Cl, no carbonic buffer and no sarcolemmal NHE (continuous lines). ROIs were placed axially at 10% from the cell ends (simulation protocol illustrated in schematic diagram at top). Solid circles indicate experimental data for pH_i gradients ($n = 22$) plotted versus the assumed value of D_{amm} (from Table 1). The experimental data are the same as those used in Fig. 6. (Bii) End-to-end pH_i gradient size calculated from panel Bi.
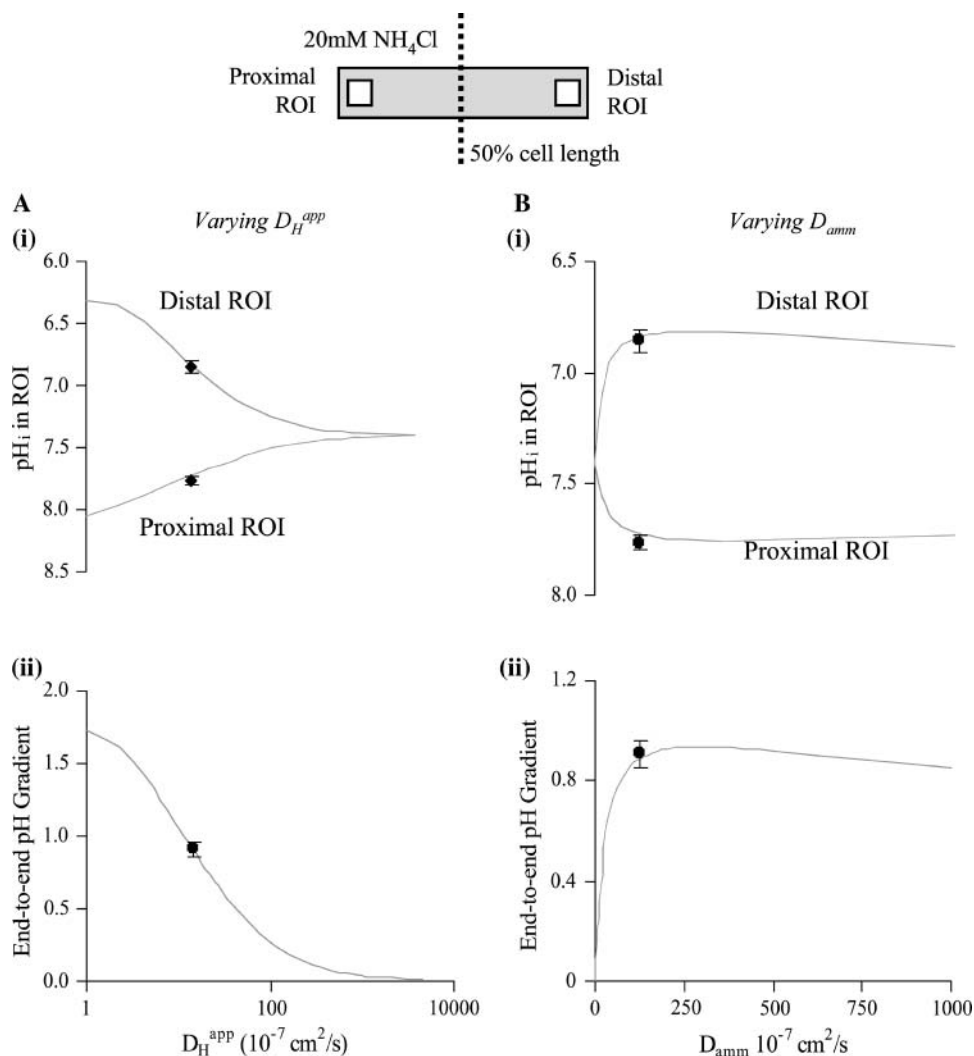
Fig. 6 B shows the results of varying D_{amm} in the model simulations. The continuous curves plotted in Fig. 6 Bi show the predicted steady-state values for pH_i in the proximal and distal ROIs. These were used to calculate the end-to-end pH_i gradient plotted in Fig. 6 Bii. As D_{amm} was raised, the end-to-end pH_i gradient showed biphasic behavior (Fig. 6 Bii). For the range of D_{amm} from 0 to ~3 × 10^{-5} cm^2/s, increasing NH_3/NH_4^+ mobility increased the pH_i gradient. The size of end-to-end pH_i gradient measured experimentally (solid symbol; 0.908 ± 0.052 pH units, $n = 22$; Fig. 6 Bii) suggests a best-fitting D_{amm} of $1.55 × 10^{-5}$ cm^2/s. This is close to the value assumed in our modeling, i.e., $1.27 × 10^{-5}$ cm^2/s (Table 1).

From Fig. 6 Bii, the range of D_{amm} that lies within the mean ± SE of the pH_i gradient size is from $0.98 × 10^{-5}$ cm^2/s to $9.6 × 10^{-5}$ cm^2/s. It has been shown, however, that in unbuffered aqueous media, the ammonium diffusion coefficient is $2.5 × 10^{-5}$ cm^2/s (Vanysek, 1999; corrected for temperature). The range of D_{amm} estimated from experimental data corresponds to a scaling of the ammonia/

ammonium diffusion coefficient by a factor between 0.39 and 3.8. It is unlikely that mobility of ammonia is elevated intracellularly, thus the lower boundary is likely to be of more interest. From the error bars for the pH_i-gradient size, one can therefore estimate that the intracellular environment may impede NH_3/NH_4^+ diffusion by no more than 61% (corresponding to a correction factor of 0.39). This is similar to the Kushmerick and Podolsky correction factor of 0.5.

It has been suggested (Nakajima et al., 1975) that macromolecular crowding depresses diffusion coefficients for Na^+, K^+, and other unbuffered solutes, by up to 90% (correction factor = 0.1), but the present work suggests that this is unlikely, at least in cardiac muscle. Indeed the Kushmerick and Podolsky factor for intracellular, unbuffered solutes is not a significant element in the current modeling, as pH_i gradients observed experimentally can be simulated, within means ± SE of pH_i measurement, for any value of correction factor ranging from 0.39 (i.e., reduced D_{amm}) to 1.0 (i.e., D_{amm} without macromolecular crowding), and 3.8 (i.e., enhanced D_{amm}). This is actually an advantage

in the modeling because the intracellular mobility of weak acids or bases need not be known to a high degree of accuracy to give reasonable pH_i simulations.

Effect of carbonic buffer

In the foregoing sections, experiments were performed using solutions buffered with Hepes. The physiological buffer is, however, CO_2/bicarbonate (also referred to as carbonic buffer). The special feature of carbonic buffer is its permeation across cell membranes as CO_2. Because the buffer is of low molecular weight, and therefore mobile, Eq. 1 predicts that D_H^{app} will increase (Junge and McLaughlin, 1987; Irving et al., 1990). Indeed Spitzer et al. (2002) and Stewart et al. (1999) found that carbonic buffer increased H_i^+ mobility in epithelial and cardiac cells by up to 5.8-fold. If this increase in D_H^{app} were applicable in this work, the relationship shown in Fig. 6 A would predict a major reduction in the size of pH_i gradients when using carbonic instead of Hepes-buffered superfusates.

Fig. 7 shows data binned for pH_i in proximal and distal ROIs, obtained under 5% CO_2/bicarbonate-buffered conditions, for a range of boundary positions. Superimposed with the data are model simulations for 20 mM ammonium perfusion in the presence and absence of CO_2/bicarbonate buffering (*thick* and *thin curves*, respectively). The data fit best the predictions of the carbonic model, but the reduction in amplitude of the end-to-end pH_i gradient in the presence of CO_2/bicarbonate buffer is much less than Fig. 6 A would predict, assuming rapid equilibration of the CO_2/bicarbonate buffer. In fact, the experimental data plotted in Fig. 7 A for carbonic buffer are not significantly different from that gathered under Hepes-buffered conditions.

Data binned for 50 $\pm$ 10% perfusion with 20 mM ammonium are presented in Fig. 7 B. Under these conditions, the presence of carbonic buffer decreased the longitudinal pH_i gradients by 12% although this was not statistically significant. Five more experiments were performed for a 50% perfusion with 20 mM ammonium under CO_2/bicarbonate buffered conditions, but in the presence of the carbonic anhydrase inhibitor, acetazolamide (100 μM). Fig. 7 B indicates that the drug had no significant effect on pH_i-gradient amplitude, although a trend in the observations again suggests a slight decrease.

During partial exposure of cells to ammonium, the CO_2/bicarbonate buffer therefore fails to produce significant pH_i-gradient dissipation.

Generating longitudinal pH_i gradients with acetate

The previous sections have described experiments performed using partial perfusion with the weak base, ammonium. The technique of dual microperfusion is, of course, not limited to permeant weak bases. A permeant weak acid can also be applied locally and, as Spitzer et al.
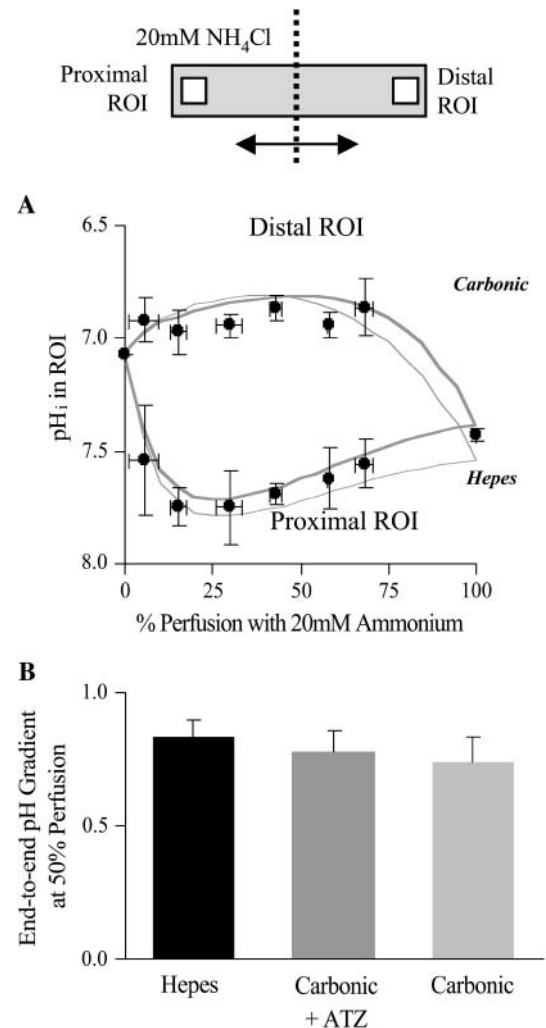

FIGURE 7 Quantifying the effect of carbonic buffer on pH_i gradient. (A) Experimental data showing the relationship between the pH_i in proximal and distal ROIs and the degree of perfusion with 20 mM ammonium under CO_2/bicarbonate-buffered condition ($n = 4, 2, 3, 4, 3, 2, 4, 11$). Experimental arrangement illustrated in schematic diagram at top. Superimposed are model predictions: thin lines, absence of carbonic buffer; thick lines, presence of carbonic buffer. (B) Histogram showing the average pH_i gradient for 50% partial perfusion with 20 mM ammonium under: i), Hepes-buffered conditions ($n = 22$); ii), CO_2/bicarbonate-buffered conditions in the presence of 100 μM acetazolamide ($n = 5$); and iii), CO_2/bicarbonate-buffered conditions ($n = 5$). Results are not significantly different at the 5% significance level.

(2000) showed with partial superfusion of propionate, the resulting pH_i gradients are, once again, considerable.

Fig. 8 illustrates an experiment where a guinea-pig myocyte was partially perfused with 80 mM sodium acetate, under Hepes-buffered conditions. The spatial distribution of steady-state pH_i is presented in the confocal images shown in Fig. 8 A. Acidosis was localized toward the proximal, exposed end (right-hand end of cell). A large end-to-end pH_i gradient was observed. This experiment has been analyzed further in Fig. 8, B and C. Intracellular pH was averaged in
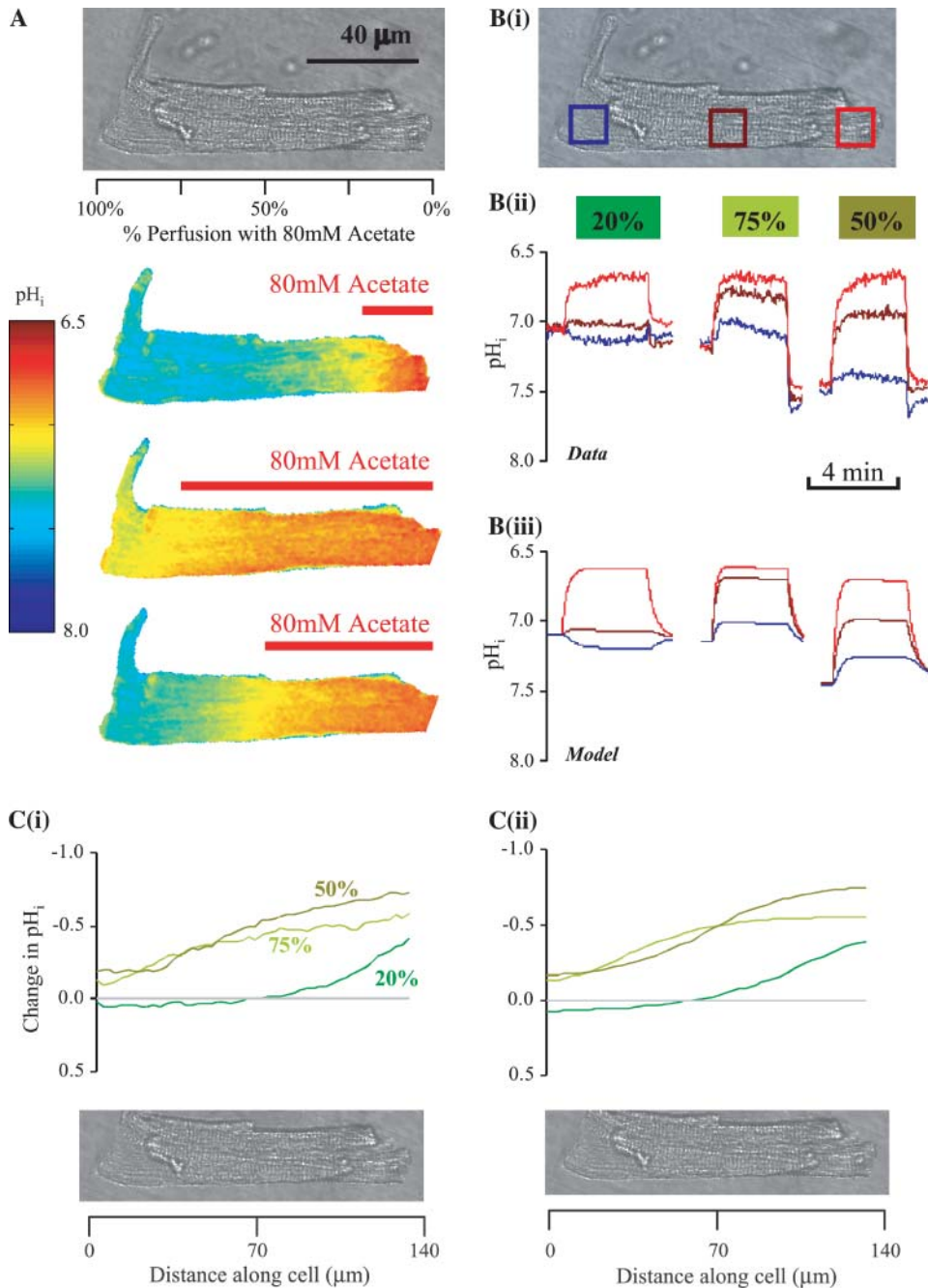
FIGURE 8 Partial exposure to acetate. (*A*, *top panel*) Transmission image of guinea-pig myocyte. (*A*, *bottom panel*) Time-averaged confocal images collected in the steady-state period during 20, 75, and 50% partial exposure of the myocyte to 80 mM acetate under Hepes-buffered conditions. (*Bi*) Transmission image of the myocyte, showing the location of ROIs within which pH_i was time averaged. (*Bii*) The experimental data, showing pH_i time courses in the three ROIs during the entire partial-perfusion experiment. (*Biii*) The time courses are simulated using diffusion-reaction algorithms, assuming no sarcolemmal NHE activity and no carbonic buffering. (*Ci*) Experimental data for the longitudinal end-to-end pH_i profiles plotted along the length of the cell during 20, 75, and 50% partial perfusion with 80 mM acetate. (*Cii*) The longitudinal pH_i profiles have been simulated using diffusion-reaction algorithms.

three ROIs (positioned as indicated in Fig. 8 *Bi*) during 20, 75, and 50% partial exposures to acetate (Fig. 8 *Bii*). The pH_i in the three ROIs attained a steady state within 30 s. The time course of pH_i changes was accurately reproduced by the diffusion-reaction model (Fig. 8 *Biii*). To test the model further, longitudinal pH_i profiles were averaged for a period of 20 s in the steady state. These averaged profiles are shown in Fig. 8 *Ci*. They are sigmoidal in shape and are also well simulated by the model (Fig. 8 *Cii*), suggesting a diffusion-reaction phenomenon. The simulations in Fig. 8 assumed no carbonic buffer and no sarcolemmal NHE activity.

Experiments similar to that described in Fig. 8 were performed using 80 mM acetate perfusion at different microstream boundary positions ($n = 40$). The steady-state pH_i in the proximal and distal ROIs during dual microperfusion was binned and plotted as a function of microstream boundary position in Fig. 9 *A*. The end-to-end pH_i gradient (difference between proximal and distal ROI pH_i) was then plotted in panel *B*. In some experiments, the microstream solutions contained 30 μM cariporide to investigate the effect of NHE inhibition on gradient size. These data were binned separately, and are represented by
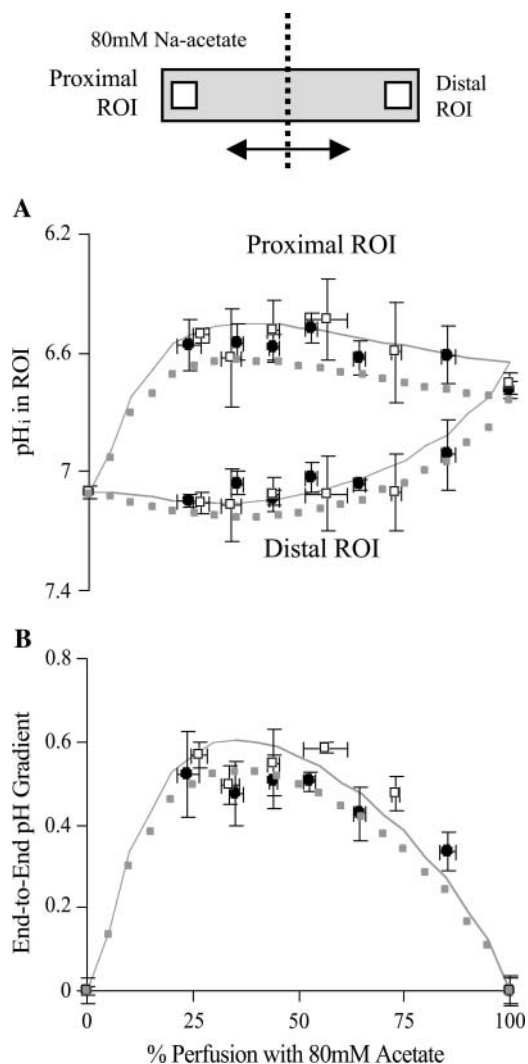
FIGURE 9 pH$_i$ gradient depends on fractional exposure to acetate. (A) The pH$_i$ in the proximal and distal ROIs is plotted as a function of percentage perfusion with 80 mM acetate. ROIs were positioned axially at 10% away from the cell ends (shown in schematic diagram at *top*). Solid symbols represent binned data ($n = 10, 4, 4, 4, 5, 3, 4, 8$) from experiments performed in the absence of cariporide in both microstreams. Open symbols ($n = 4, 3, 3, 6, 2, 2, 6$) represent experiments performed in the presence of cariporide (30 μM) in both microstreams. The continuous lines are model predictions, performed assuming no carbonic buffer and no sarcolemmal NHE activity. The dotted curves denote similar model predictions, but performed assuming NHE activity. Both curves fit the experimental data equally well. (B) End-to-end pH$_i$ gradients were calculated as the difference between the proximal and distal ROI pH$_i$. Model predictions are shown by the continuous (no NHE) and dotted (normal NHE) curves.

open symbols in Fig. 9. Superimposed on the experimental results in Fig. 9 are the outputs of two simulations. The continuous curves show predictions from a model without sarcolemmal NHE activity, whereas the dotted curves represent simulations that included NHE. In both model and experiment there was a biphasic dependence of the steady-state pH$_i$ gradient upon fractional acetate exposure, with no gradient occurring for 0 and 100% exposure, and

a maximal gradient occurring around 35%. This result therefore resembles that obtained previously with variable ammonium exposure (Fig. 3).

Experimental data presented in Fig. 9 *B* suggest that, in the presence of cariporide (to inhibit NHE), the end-to-end pH$_i$ gradient was similar to that observed under control conditions (with functional NHE). Sarcolemmal acid extrusion therefore plays little role in defining the pH$_i$ gradient, at least not during the periods of exposure (~2 min) tested in this work. Indeed, the diffusion-reaction algorithms run in the presence and absence of sarcolemmal NHE both fit the data within the tolerance of experimental error. The model predicts that the presence of sarcolemmal NHE activity will decrease the size of pH$_i$ gradients generated with 80 mM acetate by no more than 13%.

Generating longitudinal pH$_i$ gradients with carbon dioxide

As shown earlier, carbonic buffer does not significantly affect the pH$_i$ gradients generated during partial exposure to ammonium. In this section, we explore the effect of exposing a myocyte to a spatial gradient of extracellular CO$_2$. This was achieved by including a high partial pressure of CO$_2$ in one of the two microstreams.

Fig. 10 illustrates an experiment performed on a guinea-pig myocyte. The bathing solution and the left microstream contained Hepes-buffered normal Tyrode at pH 7.4. The right microstream was equilibrated with 20% CO$_2$ and contained 88 mM bicarbonate to bring the pH to 7.4. No Hepes buffer was included in this microstream. Using the Henderson-Hasselbalch equation, a solution with 20% CO$_2$/88 mM HCO$_3^-$ and pH 7.4 contains an equivalent of 4.6 mM CO$_2$ dissolved in water, either as CO$_2$(aq) or H$_2$CO$_3$(aq).

As shown in the confocal images of pH$_i$, a considerable acidosis developed in the region exposed to 20% CO$_2$. In the region not exposed to this weak acid, the pH$_i$ change was smaller, giving rise to an overall end-to-end pH$_i$ gradient of up to half a pH unit. Experiments were performed in the absence of NHE inhibitors because Fig. 9 provided convincing evidence that any effect of NHE activity was small (80 mM acetate produced similar pH displacements as 20% CO$_2$). Fig. 10 shows regional pH$_i$ time courses (Fig. 10 *Bii*) and longitudinal pH$_i$ profiles (Fig. 10 *Ci*). Again, these were closely matched by predictions of the diffusion-reaction model. The algorithm used in this section employed a hydration constant for CO$_2$ equal to that measured in cardiac myocytes with intact carbonic anhydrase activity (Leem and Vaughan-Jones, 1998). No sarcolemmal permeability to HCO$_3^-$ was included in the model, but this is likely to have been small (Leem and Vaughan-Jones, 1998).

A total of 37 experiments was performed on guinea-pig myocytes using partial perfusion with 20% CO$_2$. In these experiments, the position of the microstream boundary was varied. Binned data, together with model predictions, are
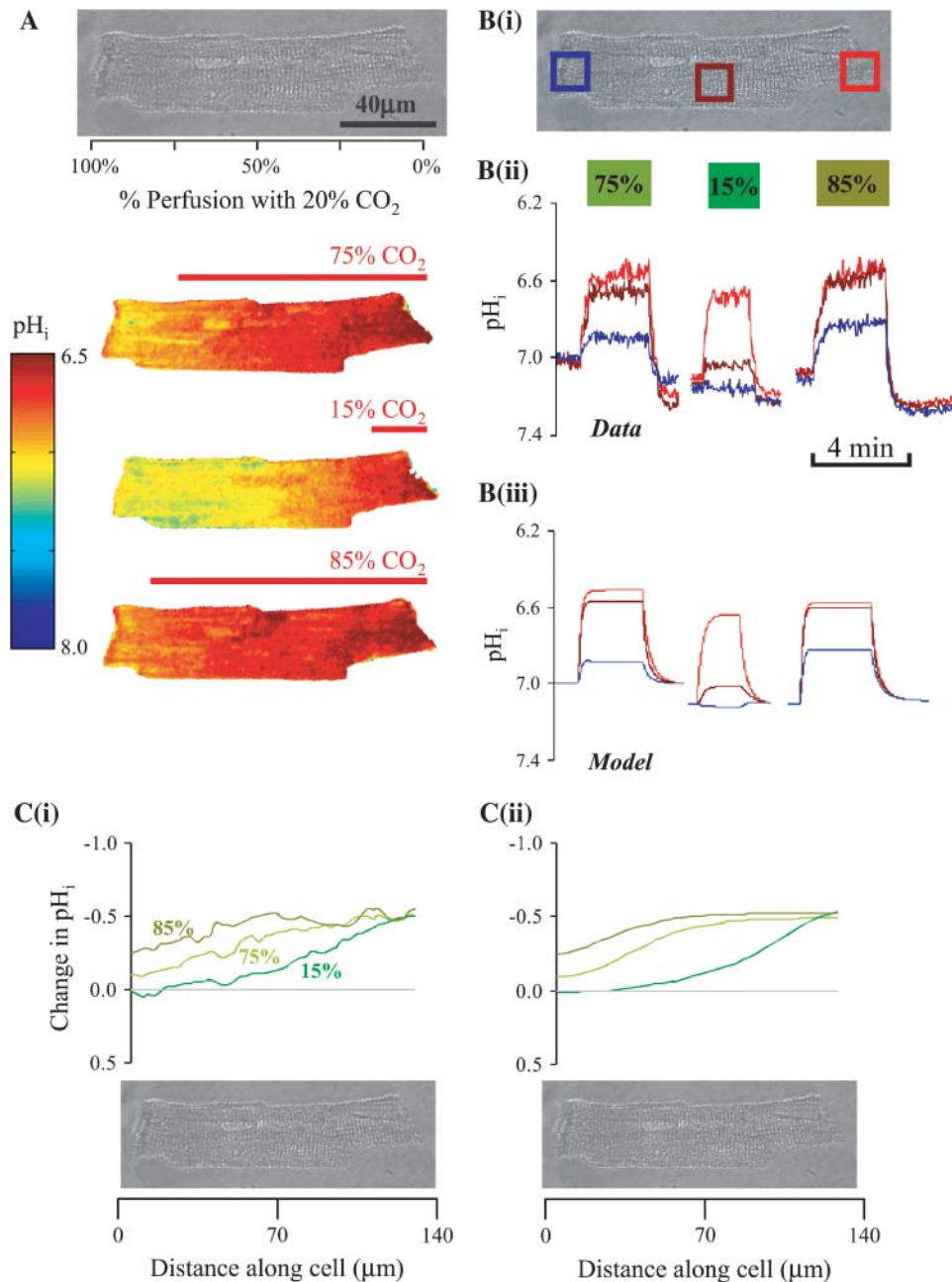
FIGURE 10 Partial exposure to high CO_2/HCO_3^-. (*A, top panel*) Transmission image of the guinea-pig myocyte used in the experiment. (*A, bottom panel*) Time-averaged confocal images collected in the steady-state period during 75, 15, and 85% partial exposure of the myocyte to 20% CO_2/ 88 mM bicarbonate. The other microstream was CO_2-free, buffered with Hepes. (*Bi*) Transmission image of the myocyte, showing the location of ROIs within which pH_i was averaged. (*Bii*) Experimental results, showing pH_i time courses in the three ROIs during the entire partial-perfusion experiment. (*Biii*) Simulation of pH_i time courses using diffusion-reaction algorithms, assuming no sarcolemmal NHE activity. (*Ci*) Experimental results for the longitudinal end-to-end pH_i profiles plotted along the length of the cell during 75, 15, and 85% partial perfusion with 20% CO_2. (*Bii*) These longitudinal pH_i profiles have been simulated using diffusion-reaction algorithms.

shown in Fig. 11. Panel *A* shows the steady-state pH_i measured in an ROI at each end of the myocyte. The end-to-end pH_i gradient is illustrated in Fig. 11 *B*. The interpretation of the results is similar to that with partial exposure to ammonia or acetic acid (Figs. 3 and 9): there is a biphasic dependence of pH_i gradient on fractional exposure to 20% CO_2, with the largest gradient (~0.6 pH units) occurring at ~35% exposure. This is comparable to the maximum gradient obtained with 80mM acetate (Fig. 9 *B*). However, with CO_2, the concentration of the applied weak acid is 16-fold lower.

The maximal effectiveness of an extracellular weak acid/base in generating a longitudinal pH_i gradient is, therefore,

20 mM NH_4Cl > 20% CO_2 > 80 mM sodium-acetate. This sequence is similar to that reported by Spitzer et al. (2000), where propionate was perfused instead of acetate.

DISCUSSION

Localization of extracellular weak acid/base induces pH_i gradients

By using a dual microstream apparatus in conjunction with an isolated ventricular myocyte, we have shown that an extracellular concentration gradient of membrane-permeant
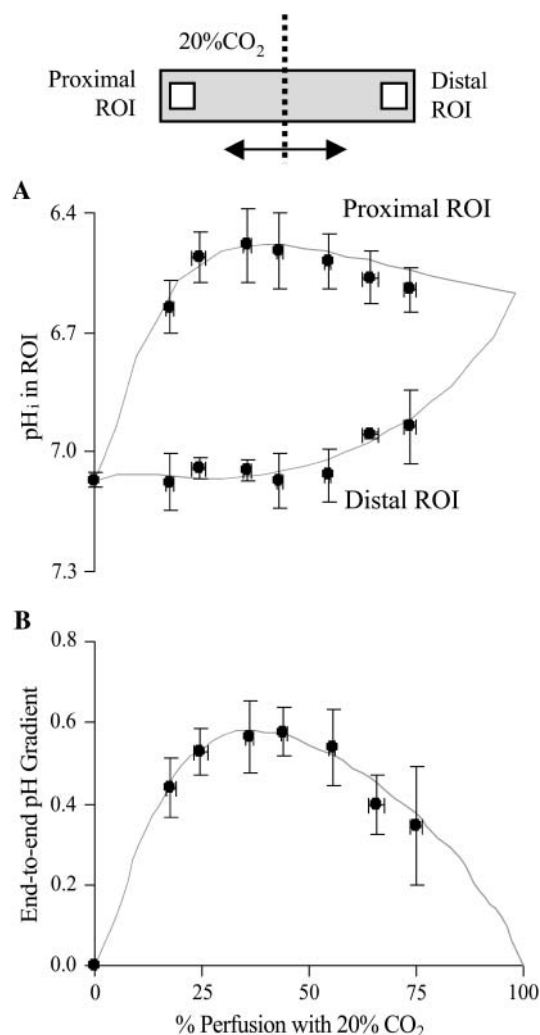
FIGURE 11 pH_i gradient depends on fractional exposure to CO_2/HCO_3^-. (*A*) The pH_i in proximal and distal ROIs is plotted as a function of percentage perfusion with 20% CO_2. The position of ROIs is depicted in the schematic diagram at top. Solid symbols represent binned data ($n = 4, 4, 4, 9, 6, 10, 2, 2$). The continuous lines are model predictions (assuming no sarcolemmal NHE activity). (*B*) End-to-end pH_i gradients were calculated as the difference between the proximal and distal ROI pH_i. Model predictions are shown by the continuous biphasic curve.

weak acid or base generates an intracellular spatial gradient of pH. Presentation of extracellular solutes such as ammonia (460 μM in 20 mM NH_4Cl), acetic acid (110 μM in 80 mM Na-acetate), and carbon dioxide (4.6 mM in 20% CO_2/88 mM HCO_3^-) to a localized region of the cell establishes a pH_i gradient, sometimes as large as 1 pH unit. This confirms the results of an earlier study on rabbit ventricular myocytes (Spitzer et al., 2000).

Intracellular proton mobility is low

The pH_i gradient established by dual microperfusion provides important information about cytoplasmic proton

movement. If one assumes that such movement is diffusive, as proposed previously (e.g., Spitzer et al., 2000; Vaughan-Jones et al., 2002), then the large spatial pH_i gradients indicate that H^+ mobility within the cytoplasmic compartment must be considerably lower than in pure water ($D_H = 1.2 \times 10^{-4}$ cm^2/s). Indeed, we have calculated (Fig. 6 *Aii*) that if the latter condition were to prevail inside the cell, the pH_i gradient would be negligible, as it would be dissipated by rapid H^+ diffusion. Previous estimates for intracellular D_H^{app} obtained from acid-injection experiments using a cell-attached micropipette (4–12.1 $\times$ 10^{-7} cm^2/s; Vaughan-Jones et al., 2002; Zaniboni et al., 2003) are comparable to the estimate of D_H^{app} predicted from the relationship shown in Fig. 6 *Aii* (14.4 $\pm$ 1.8 $\times$ 10^{-7} cm^2/s; value adjusted to a resting pH_i of 7.07). In all cases, D_H^{app} is about two orders of magnitude lower than D_H in water. This work therefore provides independent confirmation that intracellular proton mobility is remarkably low.

Dual microperfusion represents a simple and convenient means of estimating intracellular proton mobility in cardiac myocytes. It is far less invasive than using a patch pipette to localize an intracellular acid load. Although the technique depends on a mathematical algorithm to deconvolute D_H^{app} from the size and shape of the pH_i gradient, the analytical procedure has now been well tried and tested, both experimentally and theoretically. The dual microstream method therefore offers a practical solution to determining intracellular D_H^{app} without using patch-clamp technology.

The buffer hypothesis of H_i^+ mobility

Dual microperfusion provides a rigorous test of the buffer hypothesis of H_i^+ mobility. This states that spatial movement of protons in the cytoplasmic compartment is mediated almost entirely via diffusive shuttling on mobile buffers. Such buffers are likely to be molecules of moderate molecular weight ($\sim$200 Da) such as analogs of the dipeptides homocarnosine and anserine, as well as various phosphate compounds. Their combined buffer capacity (11 mM at resting pH_i; Vaughan-Jones et al., 2002) far outweighs the concentration of H_i^+ ($\sim$85 nM), and so virtually all spatial H_i^+ movement occurs via a concentration-driven movement of the buffer. Because mobile buffers have a higher molecular weight than free protons, H_i^+ mobility is low. Mobility is reduced further by the presence of fixed buffers, such as proteins, that compete with mobile buffers for protons.

In most previous work, we developed diffusion models that defined H_i^+ mobility in terms of an apparent proton diffusion coefficient, D_H^{app} (Vaughan-Jones et al., 2002; Zaniboni et al., 2003). In this work, we have modeled proton movement mechanistically in terms of buffer mobility. Although the simulations include a component accounting for the diffusion of free protons, this has little effect on the model output.

The buffer-shuttle algorithm successfully simulates local pH_i gradients generated under a wide variety of conditions. These include the local application of different species of weak acid or base, variation in the fractional exposure of a cell to these solutes, and variation in their concentration. The success of the modeling argues strongly that a combination of mobile and fixed intracellular buffers is sufficient to explain the mobility of intracellular protons.

Mechanism of pH_i gradient generation during dual microperfusion

Diffusion, reaction, and permeation fluxes for protons

Dual microperfusion induces a pH_i gradient because local exposure to extracellular acetic acid, CO_2, or ammonia produces, in effect, a local influx of acid or base. Weak acids (H$\mathbf{A}$) and weak bases ($\mathbf{B}$) are in dynamic equilibrium with their conjugate pair.

$$\mathbf{HA} \Leftrightarrow H^+ + \mathbf{A}^- \quad \text{or} \quad \mathbf{B} + H^+ \Leftrightarrow \mathbf{BH}^+.$$
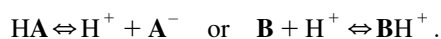
For low molecular weight solutes, the uncharged (lipophilic) form (H$\mathbf{A}$, $\mathbf{B}$) is typically far more permeant across biological membranes (NH_3, HAc, CO_2) than the charged (polar) conjugate (NH_4^+, Ac^-, HCO_3^-). The permeation steps are defined by open arrows in the diagrams shown in Fig. 12, adapted from Spitzer et al. (2000).

Once inside the cell, H$\mathbf{A}$ or $\mathbf{B}$ can, respectively, donate or bind an intracellular proton, leading to a change of pH_i in the proximal region of the cell. We define this as a reaction flux of acid equivalents. Thus, partial perfusion of ammonium chloride leads to a local rise of intracellular pH as NH_3 rapidly permeates the sarcolemma taking up intracellular protons to form ammonium ions (Fig. 12 A). Conversely, partial perfusion with sodium acetate decreases pH_i locally, as acetic acid enters the cell, releasing intracellular protons (Fig. 12 B). In the absence of CO_2/HCO_3^-, the changes of pH_i are attenuated by intrinsic buffering. They will also be dispersed spatially on the intrinsic mobile buffer shuttle. This produces, in effect, a dissipative proton flux, F_H, characterized by an apparent proton diffusion coefficient, D_H^{app}. The flux can be quantified as the difference between the flux of protonated and unprotonated mobile buffer ($J_{HMob} - J_{Mob}$). Because fixed buffers have a negligible diffusion coefficient, their contribution to F_H can be ignored. Thus, during local perfusion with ammonium chloride, protons are shuttled from distal to proximal regions (Fig. 12 A), driven by the longitudinal $[H^+]_i$ gradient. During local perfusion with sodium acetate, the $[H^+]_i$ gradient, and thus the dissipative proton flux, is reversed (Fig. 12 B).

In parallel with F_H, there is a diffusive flux of the charged and uncharged forms of weak acid or base. Because the weak acid/base and its conjugate are low molecular weight, unbuffered solutes, their intracellular mobility will be high
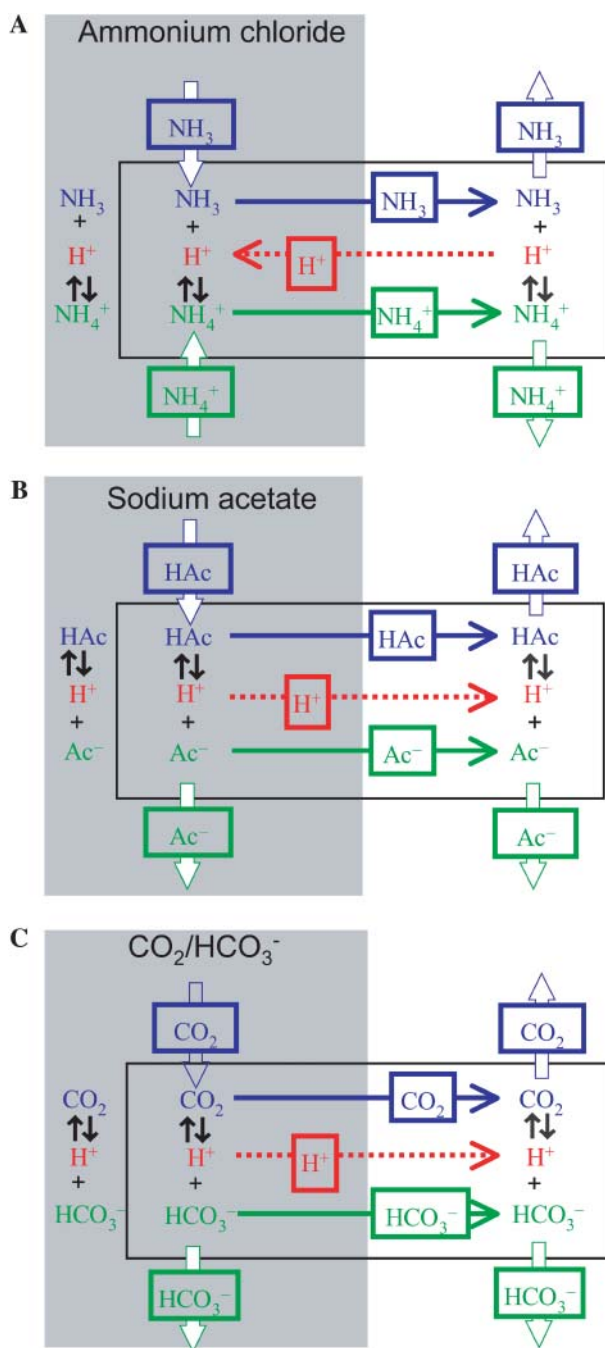

FIGURE 12 Mechanism of pH_i gradient generation during dual microperfusion. Schematic diagrams showing various solute fluxes during partial perfusion of a myocyte with (A) NH_4Cl, (B) sodium acetate, and (C) CO_2. Thick, open arrows denote sarcolemmal permeation of weak acid/base (*blue*) or its charged conjugate (*green*). Note that, in the steady state, there is an efflux of Ac^- and HCO_3^- anions from the proximal region, whereas there is an influx of NH_4^+ cations. These fluxes are directed by the negative membrane potential (-80 mV in the model). Thin, solid arrows denote intracellular diffusive flux of weak acid/base (*blue*) or its charged conjugate (*green*). Dashed arrow (*red*) shows intracellular, dissipative flux of protons. Black arrows denote reactive fluxes for weak acid/base.

compared with H_i^+ mobility. There is thus a longitudinal NH_3 and NH_4^+ flux (Fig. 12 *A*) or a longitudinal HAc and Ac^- flux (Fig. 12 *B*), from proximal to distal regions. These movements represent another form of proton-equivalent flux. This can be quantified as the difference between the flux of the protonated and unprotonated species (e.g., $J_{NH4+} - J_{NH3}$ or $J_{HAc} - J_{Ac}$). As distal regions of the cell are not exposed to extracellular weak acid/base, much of the uncharged species escapes from there, across the sarcolemma. The charged forms are less permeant, and so are trapped within the cell. They can, however, be transformed chemically, as part of a reaction flux. Thus, ammonium ions can dissociate into NH_3 (which escapes across the sarcolemma) and H^+ ions (Fig. 12 *A*). This explains the distal acidosis observed during local ammonium exposure (Fig. 3, when partial exposure is <80%) and, by a similar mechanism, the distal alkalosis observed during local acetate exposure (Fig. 9, when fractional exposure is <60%). Unlike the proton flux via intrinsic mobile buffer, which seeks to dissipate the pH_i gradient, the intracellular proton flux via exogenous weak acid/base is generative, as it tends to increase the gradient.

A steady-state pH_i gradient will be achieved when the longitudinal dissipative and generative fluxes of proton equivalents are matched by the transmembrane entry of weak acid or base at the locally exposed end of the cell. A low value for D_H^{app} will result in a large pH_i gradient whereas a high D_H^{app} will induce a small gradient. This is demonstrated in the model (Fig. 6 *A*) where simulating a 10-fold increase of D_H^{app} (produced by increasing D_{mob}) collapsed the pH_i gradient by a factor of 4.2.

Factors that influence the pH$_i$ gradient

Species and concentration of weak acid/base

The size of the pH_i gradient depends, in part, on the species of weak acid/base that is locally applied. When the gradient (Figs. 3, 9, and 11) is normalized to the total extracellular concentration of weak acid/base, the sequence is: NH_4Cl > $NaAc$ > CO_2. The position of CO_2 at the end of this sequence may be explained by the slow equilibration of carbonic buffer. Indeed, by increasing the rate constant of hydration (k_{hydr}) in the mathematical algorithm, larger pH_i gradients are predicted for the same concentration of CO_2 (results not shown). NH_4Cl has the highest potency because ammonia has a high membrane permeability (cf. Table 1) and its pK is closer to extracellular pH than that for acetic acid, thus enhancing the concentration of the membrane-permeant form. The size of the pH_i gradient also depends on the overall concentration of extracellular weak acid or base, as illustrated for NH_4Cl in Fig. 5. Thus, a combination of concentration, membrane permeability, and pK of a weak acid/base governs the rate at which acid equivalents can be introduced into the exposed end of the cell.

Carbonic buffer

Local exposure to CO_2 produces a pH_i gradient by a mechanism comparable to that discussed above for ammonia and acetic acid. This is illustrated in Fig. 12 *C*. The continuous entry and hydration of CO_2 acidifies proximal regions, setting up a pH_i gradient that initiates a dissipative proximal-to-distal flux of acid, in parallel with fluxes of CO_2 and HCO_3^-. The HCO_3^- flux represents a form of facilitated CO_2 diffusion (Geers and Gros, 2000), as some CO_2 in proximal regions converts to HCO_3^- that diffuses distally and then converts back into CO_2.

Given that local CO_2 exposure induces a large pH_i gradient (up to 0.6 pH_i units; see Fig. 11 *B*), it was surprising that uniform superfusion of carbonic buffer had little effect on pH_i gradients formed during local ammonium exposure. As both CO_2 and HCO_3^- are mobile, one would expect them to mediate a dissipative intracellular acid flux, analogous to that produced by intrinsic buffer. Indeed, previous work has shown that carbonic buffer facilitates passive H_i^+ mobility by a factor of 2.5–5.8 (Zaniboni et al., 2003; Spitzer et al., 2002). Despite this, our diffusion-reaction model predicted only a small gradient reduction, in agreement with experimental observations (Fig. 7).

The analysis presented in Fig. 13 helps to explain the above paradox. Intracellular diffusive H^+ fluxes have been computed across a planar surface at the middle of a model cell (Fig. 13, *A* and *B*, *insets*, *red surface*), during local exposure to ammonia or acetic acid, in the uniform presence of CO_2/HCO_3^- buffer. As discussed earlier, the intrinsic and carbonic buffer shuttles tend to dissipate the pH_i gradient whereas the NH_3/NH_4^+ or HAc/Ac^- shuttle is generative. The dissipative proton flux in the steady state (i.e., the sum of the intrinsic mobile and carbonic buffer shuttles) is large (102 mM/min in Fig. 13 *A*, and 33 mM/min in Fig.13 *B*). The flux carried by carbonic buffer, however, is only a small fraction of this, stabilizing at 4–8 mM/min. Thus, this buffer will play only a minor role in limiting the size of the end-to-end pH_i gradient. The model predicts that superfusing carbonic buffer will reduce the amplitude of the pH_i gradient by ~10% during local ammonium exposure and ~20% during local acetate exposure. Such reductions may be difficult to resolve experimentally.

The factor limiting the dissipative proton flux carried on the carbonic shuttle appears to be the chemical hydration/dehydration of CO_2. Modeling a 10-fold increase in the rate constant for this reaction results in a 40% collapse of the pH_i gradient induced by local ammonium exposure (results not shown). The facilitation of H_i^+ mobility by carbonic buffer will be set by the level of expression of the endogenous catalyst, carbonic anhydrase (CA). It is notable, therefore, that the functional expression of CA in heart is modest, enhancing the speed of carbonic buffering by only 2.5-fold (Leem and Vaughan-Jones, 1998).
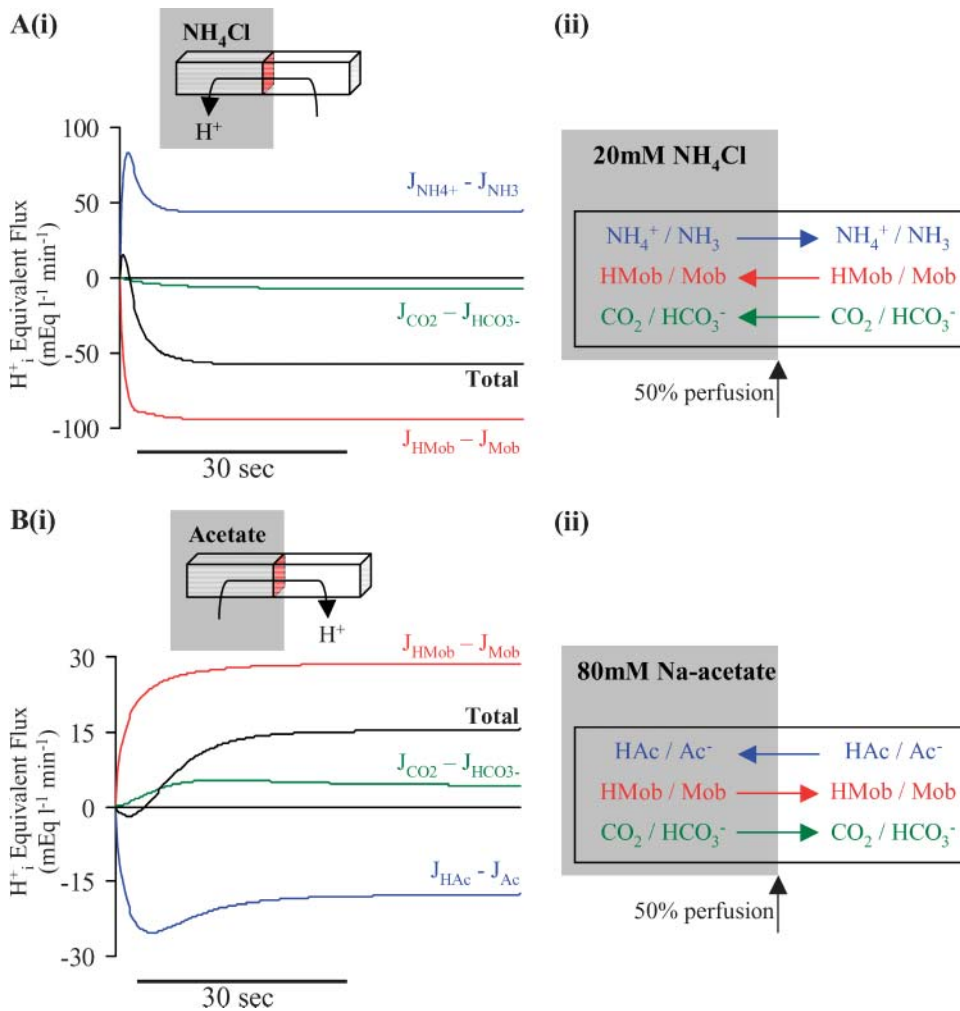
FIGURE 13 Flux analysis during dual microperfusion. (*Ai*) Time course of proton-equivalent fluxes during partial exposure of a cell to NH_4Cl. Model simulations were run for 60 s during a 50% partial exposure to 20 mM NH_4Cl under uniform superfusion with 5% CO_2/22 mM bicarbonate-buffered solutions. The models were used to calculate the proton fluxes carried by three shuttles, as illustrated schematically in right-hand panel. (*Aii*) The shuttles are for mobile buffer (*red*), carbonic buffer (*green*), and NH_4^+/NH_3 (*blue*). Fluxes were calculated over the cross-sectional area, marked red in the inset. The inset also illustrates the net direction of proton flux in the steady state. NHE activity was not included in the modeling. (*Bi*) Time course of proton-equivalent fluxes during partial exposure of a cell to sodium acetate. Model simulations were run for 60 s during a 50% partial exposure to 80 mM sodium acetate under uniform superfusion with 5% CO_2/22 mM bicarbonate-buffered solutions (no NHE activity). A similar analysis to that in part *A* was performed for the three types of shuttle flux listed in panel *Bii*, i.e., for intrinsic mobile buffer, carbonic buffer, and for HAc/Ac^-. Inset shows net direction of movement of protons in the steady state.

In previous work where a pH_i gradient was set up using acid injection from a glass micropipette, the injection flux was relatively small, being ~8 mM/min (Vaughan-Jones et al., 2002). Under these conditions, carbonic buffer significantly contributed to the dissipation of the intracellular pH gradient (Spitzer et al., 2002). The ability of carbonic buffer to collapse a pH_i gradient therefore depends on the magnitude of the acid-equivalent flux that sets up the pH_i disturbance; it is particularly effective during low rates of acid or base loading.

Sarcolemmal NHE activity

The apparent lack of effect of sarcolemmal NHE activity on the pH_i gradient is, like the lack of effect of carbonic buffer described above, related to the size of the diffusive proton flux. During local weak acid/base exposure, we estimate that sarcolemmal acid extrusion, when averaged over the whole cell surface is modest (up to 5 mM/min) compared with the dissipative flux on the intrinsic buffer shuttle (30–100 mM/min). The NHE flux will therefore exert little influence on the size of the pH_i gradient. Similar arguments apply to a lack of

effect of other sarcolemmal transporters such as Cl^--HCO_3^- exchange, Cl^--OH^- exchange, and Na^+-HCO_3^- cotransport. Local exposure of a cell to permeant weak acid/base, thus, short circuits the ability of sarcolemmal transporters to regulate pH_i, leading to a persistent nonuniformity of pH_i.

Stability of pH_i gradient

The persistence of the pH_i gradient during dual microperfusion (over several minutes in this work) contrasts with the transient pH_i response to a uniform extracellular exposure to weak acid/base, a phenomenon that largely reflects the activity of sarcolemmal pH_i-regulatory transporters (see, e.g., Lagadic Gossmann et al., 1992; Leem et al., 1999). During local exposure, the net dissipative H^+ flux, obtained by summing all the intracellular proton fluxes, is sustained by continuous weak acid/base entry in proximal regions, and exit in distal regions (illustrated in the schematic diagrams shown in Fig. 13, *Ai* and *Bi*). It is the continuous nature of this flux that ensures a stable pH_i gradient over time. As noted in the Results, baseline pH_i may slowly drift with time, but the pH_i gradient superimposed on this remains of

constant amplitude. Slow drift, when it occurs, is reproduced accurately by the diffusion-reaction algorithm (see, e.g., Figs. 3, 9, and 11), where it is caused by slow permeation of the charged form of the weak acid/base.

Microstream boundary position

The magnitude of the pH_i gradient changed when the microstream boundary position was varied (Figs. 3, 9, and 11). The relationship was biphasic with no gradient occurring at 0 and 100% exposure to weak acid or base, and a maximal gradient occurring with intermediate exposure. The experimental data were reproduced well by the model, which predicts that a maximal gradient will occur when approximately one-third of the cell is exposed to weak acid/base. One may ask why the relationship is not centered at 50% exposure. The answer is that a highly localized acid or base influx (i.e., with <50% exposure to weak acid or base) predisposes that region of the cell to a large pH_i displacement. Under these conditions, weak acid/base entry is kept high because of the large, unexposed cytosolic volume into which it can dissipate. In contrast the ability of intrinsic mobile buffers to collapse the pH_i gradient is maximal during 50% weak acid/base exposure (when their ability either to capture or release protons is optimized). The maximal pH_i gradient therefore falls between these limits, i.e., at ~30% exposure.

Cell geometry

The elongated, flattened shape of cardiac myocytes means that they readily support longitudinal pH_i gradients in response to local acid or base loading. Fig. 4 shows that, for a given local ammonium exposure, the longer the cell the greater the pH_i gradient—an effect that was independent of boundary position. This is related to the fact that diffusion time increases with the square of distance. The geometry of a cell is therefore a key parameter in determining the size of a pH_i gradient, as suggested previously from computational modeling of pH_i gradients in various cell types, including cardiac, epithelial, and neuronal cells (Swietach et al., 2003). Diffusion time also explains why the peak pH_i gradient occurs at lower fractional exposures in longer cells, as predicted in the simulations shown in Fig. 4. Larger diffusion distances mean that the relative importance of mobile buffer versus weak acid/base flux is shifted in favor of the latter.

Physiological implications

Localization of weak acid during myocardial ischemia

In this work, a pH_i gradient was generated by spatially localizing an extracellular permeant weak acid or base. In the myocardium in vivo, spatial concentration gradients of weak acid or base will most likely occur when there is heterogeneity of vascular perfusion. An extreme example

of this would be regional ischemia. The partial pressure of CO_2 can be as high as 40% (320 mmHg) in an ischemic myocardial zone compared to 5% (40 mmHg) in normally perfused myocardium (Case et al., 1979; Cascio et al., 1992). High local levels of CO_2 are generated when lactic acid, produced in the ischemic zone, reacts with bicarbonate anions. A smooth gradient of $[CO_2]$ therefore forms between ischemic and nonischemic zones as CO_2 diffuses away. Considerable concentration differences will also exist for lactic acid, provided its principal site of production is within the ischemic zone.

In experimental models of regional ischemia, the most pronounced gradients in pH_o, K_o^+, CO_2, and other cell parameters have been observed at the edges of the ischemic zone (i.e., the border zone) Such experimental models include regional block of vascular perfusion in pig hearts (Coronel et al., 1995), in isolated rabbit septa (Wilensky et al., 1986), and in papillary muscle (Cascio et al., 1992). Wilensky et al. (1986) found that the sharpest transition from normal to ischemic myocardium occurred over a width of only 130–650 μm. Extracellular pH fell from 7.4 to 6.6, suggesting that steep gradients of CO_2 may occur over a distance of 1–4 myocyte lengths. The properties of such narrow border zones have been explored experimentally in monolayers of cultured cardiomyocytes exposed to two streams of superfusate, one at pH 7.4 and the other at pH 6.5 (Hyatt et al., 1998). Using fluorescence measurements of pH_i, it was found that there was a parallel gradation of intracellular pH between the two regions. The transition distance of intracellular pH between the acidic and normal environments was 220–230 μm, i.e., around two cell lengths. The spatial gradients of CO_2 and lactate at ischemic border zones may therefore be associated with a significant nonuniformity of pH_i. We have shown recently that localization of weak acid or base at one end of an isolated ventricular cell pair can induce a profound gradient of pH_i down both cells, sustained by the translocation of protons through gap junctions (Swietach and Vaughan-Jones, 2004). Steep spatial gradients of myocardial pH_i at border zones may therefore be a hallmark of regional ischemia.

Given that there are close links between pH_i and Ca_i^{2+} in the heart, it is of interest that the ischemic border zone also appears to be a site of significant Ca_i^{2+} heterogeneity, in the form of emergent Ca^{2+} waves (Oyamada et al., 2001; Tanaka et al., 2002; Tsuiji et al., 2003). Whether pH_i heterogeneity in this region plays a role in the induction of such Ca_i^{2+} disturbances remains to be determined.

Role of carbonic buffer in limiting pH_i-gradient formation

Our experiments involving CO_2/HCO_3^- buffer have shed new light on its importance in minimizing pH gradients inside cells during a local acid/base disturbance. As discussed earlier, facilitation of H_i^+ mobility by carbonic

buffer is a rate-dependent phenomenon. Because the functional effects of CA in heart are modest (Leem and Vaughan-Jones, 1998), carbonic facilitation of H_i^+ mobility occurs during slow but not fast acid/base disturbances. Partial exposure of myocytes to weak acids and bases, as described by Spitzer et al. (2000) and in this work, is one example of a fast pH_i disturbance. Another example, in a different cell type, would appear to be the large channel-mediated efflux of protons during severe membrane depolarization in molluscan neurons (Schwiening and Willoughby, 2002). In both cases, carbonic buffer appears to exert little or no effect on the resulting pH_i nonuniformity. On the other hand, activation of a transmembrane proton transporter will induce a slower pH_i disturbance if it mediates a lower proton flux. This would seem to be the case in duodenal enterocytes where proton influx through oligopeptide-coupled transporters (PepT-1) induces a subapical cytoplasmic acidification that is greatly reduced by the presence of carbonic buffer (Stewart et al., 1999). These results emphasize that carbonic buffer's contribution to the regulation of H_i^+ mobility and hence to the control of pH_i nonuniformity is not a constant factor.

In the presence of carbonic buffer, the ability of CA to enhance H^+-equivalent membrane transport on HCO_3^- carriers such as Na^+-HCO_3^- cotransport (Loiselle et al., 2004) and Cl^--HCO_3^- (Sterling et al., 2001) may be related to its enhancement of H_i^+ mobility (Stewart et al., 1999; Spitzer et al., 2002) given that, at least in the cardiac myocyte, activity of the transporters is regulated by pH_i and pH_o (Leem et al., 1999; Ch'en and Vaughan-Jones, 2001). CA, in combination with carbonic buffer, may thus be important for dissipating local pH microdomains close to the surface of H^+-equivalent transport proteins. This would seem reasonable in cardiac cells where many instances of sarcolemmal H^+ transport would fall into the category of a slow acid/base disturbance.

Intracellular diffusion of unbuffered solutes

During the course of this work, we were able to assess the scaling factor that accounts for the effects of macromolecular crowding on a solute's intracellular diffusion coefficient (Kushmerick and Podolsky, 1969). The original work suggested that, in muscle cells, intracellular diffusion coefficients are halved due to the reduction in the effective cell volume for diffusion. In the current work we attempted to resolve this factor for the ammonium ion. Although the experimental data had a large mean $\pm$ SE, a lower limit could be derived. This suggested that a ventricular myocyte's cytoplasmic compartment is not likely to retard the mobility of unbuffered species (such as NH_4^+) by >60% of the value measured in pure water. This should be compared with the more powerful retardation of H_i^+ mobility, an ion that is strongly buffered. Unbuffered solutes of low molecular weight therefore exhibit an intracellular mobility not greatly dissimilar to that in water.

CONCLUSIONS

Intrinsic buffering in the cytoplasmic compartment of cardiac myocytes is high, and represents a first line of defense against acid/base disturbances. Intrinsic buffering, however, results in a low H_i^+ mobility, with the possibility of significant nonuniformity of pH_i during local acid/base disturbances. This work shows that extracellular concentration gradients of permeant weak acid or base give rise to large and sustained gradients of pH_i. The properties of these pH_i gradients are well described by diffusion-reaction phenomena for mobile and fixed intracellular buffers and are consistent with a low H_i^+ mobility. The gradients are remarkably resistant to the activity of classical H^+-equivalent membrane transport mechanisms or to the CO_2/HCO_3^- buffer system. Given that spatial nonuniformity of permeant weak acid occurs in the heart during regional ischemia, this condition may be similarly associated with steep spatial gradients of myocardial pH_i.

REFERENCES

Al-Baldawi, N. F., and R. F. Abercrombie. 1992. Cytoplasmic hydrogen ion diffusion coefficient. *Biophys. J.* 61:1470–1479.

Allen, D. G., and C. H. Orchard. 1987. Myocardial contractile function during ischaemia and hypoxia. *Circ. Res.* 60:153–168.

Bountra, C., and R. D. Vaughan-Jones. 1989. Effect of intracellular and extracellular pH on contraction in isolated, mammalian cardiac muscle. *J. Physiol.* 418:163–187.

Bountra, C., K. Kaila, and R. D. Vaughan-Jones. 1988. Effect of repetitive activity upon intracellular pH, sodium and contraction in sheep cardiac Purkinje fibres. *J. Physiol.* 398:341–360.

Cascio, W. E., G. X. Yan, and A. G. Kleber. 1992. Early changes in extracellular potassium in ischemic rabbit myocardium. The role of extracellular CO_2 accumulation and diffusion. *Circ. Res.* 70:409–422.

Case, R. B., A. Felix, and F. S. Castellana. 1979. Rate of rise of myocardial PCO_2 during early myocardial ischemia in the dog. *Circ. Res.* 45:324–330.

Ch'en, F. T., and R. D. Vaughan-Jones. 2001. Na^+-HCO_3^- transport is instructed by pH and not bicarbonate or Na^+. *Biophys. J.* 80:74. (Abstr.).

Choi, H. S., A. W. Trafford, C. H. Orchard, and D. A. Eisner. 2000. The effect of acidosis on systolic Ca^{2+} and sarcoplasmic reticulum calcium content in isolated rat ventricular myocytes. *J. Physiol.* 529:661–668.

Coronel, R., F. J. Wilms-Schopman, J. W. Fiolet, T. Opthof, and M. J. Janse. 1995. The relation between extracellular potassium concentration and pH in the border zone during regional ischemia in isolated porcine hearts. *J. Mol. Cell. Cardiol.* 27:2069–2073.

Eigen, M. 1964. Proton transfer, acid-base catalysis, and enzymatic hydrolysis. Part I. Elementary processes. *Ang. Chemie Int. Ed.* 3:1–19.

Elliott, A. C., G. L. Smith, and D. G. Allen. 1994. The metabolic consequences of an increase in the frequency of stimulation in isolated ferret hearts. *J. Physiol.* 474:147–159.

Ellis, D., and R. C. Thomas. 1976. Microelectrode measurement of the intracellular pH of mammalian heart cells. *Nature*. 262:224–225.

Forster, R. E. 1969. The rate of CO_2 equilibration between red cells and plasma. *In* CO_2: Chemical, Biochemical and Physiological Aspects. R. E. Forster, J. T. Edsall, A. B. Otis, and F. J. W. Roughton, editors. SP-188, NASA, Washington, DC. 275–286.

Gabso, M., E. Neher, and M. E. Spira. 1997. Low mobility of the Ca^{2+} buffers in axons of cultured Aplysia neurons. *Neuron*. 18:473–481.

Garlick, P. B., G. K. Radda, and P. J. Seeley. 1979. Studies of acidosis in the ischaemic heart by phosphorus nuclear magnetic resonance. *Biochem. J*. 184:547–554.

Geers, C., and G. Gros. 2000. Carbon dioxide transport and carbonic anhydrase in blood and muscle. *Physiol. Rev*. 80:681–715.

Harned, H. S., and F. C. Hickey. 1937. The ionisation of acetic acid in aqueous sodium chloride solutions from 0 to 40°C. *J. Am. Chem. Soc*. 59:1284–1288.

Harrison, S. M., J. E. Frampton, E. McCall, M. R. Boyett, and C. H. Orchard. 1992. Contraction and intracellular Ca^{2+}, Na^+ and H^+ during acidosis in rat ventricular myocytes. *Am. J. Physiol*. 262:C348–C357.

Hyatt, C. J., J. J. Lemasters, B. J. Muller-Borer, T. A. Johnson, and W. E. Cascio. 1998. A superfusion system to study border zones in confluent cultures of neonatal rat heart cells. *Am. J. Physiol*. 274:H2001–H2008.

Irving, M., J. Maylie, N. L. Sizto, and W. K. Chandler. 1990. Intracellular diffusion in the presence of mobile buffers. Application to proton movement in muscle. *Biophys. J*. 57:717–721.

Junge, W., and S. McLaughlin. 1987. The role of fixed and mobile buffers in the kinetics of proton movement. *Biochim. Biophys. Acta* 890:1–5.

Klocke, R. A., K. K. Anderson, H. H. Rotman, and R. E. Forster. 1972. Permeability of human erythrocytes to ammonia and weak acids. *Am. J. Physiol*. 222:1004–1013.

Komukai, K., F. Brette, C. Pascarel, and C. H. Orchard. 2002. Electrophysiological response of rat ventricular myocytes to acidosis. *Am. J. Physiol*. 283:H412–H422.

Kushmerick, M. J., and R. J. Podolsky. 1969. Ionic mobility in muscle cells. *Science*. 166:1297–1298.

Lagadic-Gossmann, D., K. J. Buckler, and R. D. Vaughan-Jones. 1992. Role of bicarbonate in pH recovery from intracellular acidosis in the guinea-pig ventricular myocyte. *J. Physiol*. 458:361–384.

Leem, C. H., and R. D. Vaughan-Jones. 1998. Out-of-equilibrium pH transients in the guinea-pig ventricular myocyte. *J. Physiol*. 509:471–485.

Leem, C. H., D. Lagadic-Gossmann, and R. D. Vaughan-Jones. 1999. Characterization of intracellular pH regulation in the guinea-pig ventricular myocyte. *J. Physiol*. 517:159–180.

Loiselle, F. B., P. E. Morgan, B. V. Alvarez, and J. R. Casey. 2004. Regulation of the human NBC3 Na^+/HCO_3^- cotransporter by carbonic anhydrase II and PKA. *Am. J. Physiol*. 286:C1423–C1433.

Nakajima, S., Y. Nakajima, and J. Bastian. 1975. Effects of sudden changes in external sodium concentration on twitch tension in isolated muscle fibers. *J. Gen. Physiol*. 65:459–482.

Oyamada, M., E. Tsujii, H. Tanaka, T. Matsushita, and T. Takamatsu. 2001. Abnormalities in gap junctions and Ca^{2+} dynamics in cardiomyocytes at the border zones of myocardiac infarcts. *Cell Commun. Adhes*. 8:335–338.

Reid, R. C., J. M. Prausnitz, and T. K. Sherwood. 1987. Properties of Gases and Liquids, Table H-7. McGraw-Hill Publishers, New York.

Roos, A., and W. F. Boron. 1981. Intracellular pH. *Physiol. Rev*. 61:296–434.

Satoh, H., L. M. Delbridge, L. A. Blatter, and D. M. Bers. 1996. Surface:volume relationship in cardiac myocytes studied with confocal microscopy and membrane capacitance measurements: species-dependent and developmental effects. *Biophys. J*. 70:1494–1504.

Scholz, W., U. Albus, L. Counillon, H. Gogelein, H. J. Lang, W. Linz, A. Weichert, and B. A. Scholkens. 1995. Protective effects of HOE642, a selective sodium-hydrogen exchange subtype 1 inhibitor, on cardiac ischaemia and reperfusion. *Cardiovasc. Res*. 29:260–268.

Schwiening, C. J., and D. Willoughby. 2002. Depolarisation induced pH microdomains and their relationship to calcium transients in isolated snail neurons. *J. Physiol*. 538:371–382.

Spitzer, K. W., and J. H. B. Bridge. 1989. A simple device for rapidly exchanging solution surrounding a single cardiac cell. *Am. J. Physiol*. 256:C441–C447.

Spitzer, K. W., P. R. Ershler, R. L. Skolnick, and R. D. Vaughan-Jones. 2000. Generation of intracellular pH gradients in single cardiac myocytes with a microperfusion system. *Am. J. Physiol*. 278:H1371–H1382.

Spitzer, K. W., R. L. Skolnick, B. E. Peercy, J. P. Keener, and R. D. Vaughan-Jones. 2002. Facilitation of intracellular H^+ ion mobility by CO_2/HCO_3- in rabbit ventricular myocytes is regulated by carbonic anhydrase. *J. Physiol*. 541:159–167.

Sterling, D., R. A. Reithmeier, and J. R. Casey. 2001. A transport metabolon: functional interaction of carbonic anhydrase II and chloride/bicarbonate exchangers. *J. Biol. Chem*. 276:47886–47894.

Stewart, A. K., C. A. R. Boyd, and R. D. Vaughan-Jones. 1999. A novel role for carbonic anhydrase: pH gradient dissipation in mouse small intestinal enterocytes. *J. Physiol*. 516:209–217.

Swietach, P., and R. D. Vaughan-Jones. 2004. Novel method for measuring junctional proton permeation in isolated ventricular myocyte cell pairs. *Am. J. Physiol*. In press.

Swietach, P., M. Zaniboni, A. K. Stewart, A. Rossini, K. W. Spitzer, and R. D. Vaughan-Jones. 2003. Modelling intracellular H^+ ion diffusion. *Prog. Biophys. Mol. Biol*. 83:69–100.

Tanaka, H., M. Oyamada, E. Tsujii, T. Nakajo, and T. Takamatsu. 2002. Excitation-dependent intracellular Ca^{2+} waves at the border zone of the cryo-injured rat heart revealed by real-time confocal microscopy. *J. Mol. Cell. Cardiol*. 34:1501–1512.

Thomas, J. A., R. N. Buchsbaum, A. Zimniak, and E. Racker. 1979. Intracellular pH measurements in Ehrlich ascites tumor cells utilising spectroscopic probes generated in situ. *Biochemistry*. 18:2210–2218.

Tsuiji, E., H. Tanaka, M. Oyamada, K. Fujita, T. Hamamoto, and T. Takamatsu. 2003. In situ visualisation of intracellular Ca^{2+} dynamics at the border of the acute myocardiac infarct. *Mol. Cell. Biochem*. 248:135–139.

Vanysek, P. 1999. Ionic conductivity and diffusion at infinite dilution. *In* CRC Handbook of Chemistry and Physics, 79th Ed. Section 5: Thermochemistry, Electrochemistry and Kinetics. D. R. Lide, editor. CRC Press, London. 93–95.

Vaughan-Jones, R. D., B. E. Peercy, J. P. Keener, and K. W. Spitzer. 2002. Intrinsic H^+ ion mobility in the rabbit ventricular myocyte. *J. Physiol*. 541:139–158.

Wilensky, R. L., J. Tranum-Jensen, R. Coronel, A. A. Wilde, J. W. Filet, and M. J. Janse. 1986. The subendocardial border zone during acute ischaemia of the rabbit heart: an electrophysiologic, metabolic and morphologic correlative study. *Circulation*. 74:1137–1146.

Willoughby, D., and C. J. Schwiening. 2002. Electrically evoked dendritic pH transients in rat cerebellar Purkinje cells. *J. Physiol*. 544:487–499.

Yamamoto, T., P. Swietach, A. Rossini, S. H. Loh, R. D. Vaughan-Jones, and K. W. Spitzer. 2004. Functional diversity of electrogenic $Na^+-HCO_3^-$ co-transport in ventricular myocytes from rat, rabbit and guinea-pig. *J. Physiol*. 562:455–475.

Zaniboni, M., P. Swietach, A. Rossini, T. Yamamoto, K. W. Spitzer, and R. D. Vaughan-Jones. 2003. Intracellular proton mobility and buffering power in cardiac ventricular myocytes from rat, rabbit, and guinea pig. *Am. J. Physiol*. 285:H1236–H1246.